

Possible linkages between Microseisms in the Andaman-Nicobar region and Swells in the South Indian Ocean

R. Reddy^{1,2}, P. Dewangan^{1*}, P. K. Bhaskaran² and P.N.S. Roy²

¹CSIR-National Institute of Oceanography, Dona Paula, Goa – India – 403004.

²Indian Institute of Technology Kharagpur, Kharagpur, West Bengal, India – 721302

*Corresponding author Email: pdewangan@nio.org

Abstract

Microseism source characterization and its genesis play a key role in linking microseism records to prevailing atmospheric and oceanic conditions. In the present study, we analyzed the spatial and temporal distribution of microseisms in the Andaman and Nicobar region using ocean-bottom seismometers (OBSs) and nearby continental stations data for the deployment period (January 2014 to April 2014). We attempted to establish a linkage between microseisms and ocean wave parameters derived from the ERA-5 dataset.. The short-period secondary microseisms (2 – 5 s) show marked difference as compared to long-period secondary microseisms (6 – 10 s) and are associated with local climatology and geomorphology. In contrast, long-period microseisms are related to distant sources in the South Indian Ocean. The primary microseisms (11-20 s) are weak in the Andaman region and do not correlate with any ocean wave parameters.

Keywords: Microseisms, Significant Wave Height, Ocean Bottom Seismometer, Andaman and Nicobar Islands

Introduction

Microseisms are the most energetic band observed in a seismic noise spectrum. Microseisms occur due to the interaction between the solid earth and ocean-wave and their genesis depends on atmospheric and oceanic conditions, which vary spatially and temporarily. Microseisms can be broadly categorized into primary microseism (PM) or single frequency microseism with periods of 11 to 20 s and secondary microseism (SM) or double frequency (DF) microseism with periods of 2 to 10 s. The DF microseisms can be further categorized into short-period double frequency (SPDF) and long-period double frequency (LPDF) microseisms with periods of 2-5 s and 6-10 s, respectively (Stephen et al., 2003; Bromirski et al., 2005; Sun et al., 2013; Koper and Burlacu, 2014). PM originates in shallow waters, where the wavelength of wind-induced ocean surface gravity waves is greater than the water depth (Hasselmann, 1963; Haubrich and McCamy, 1969; Bromirski et al., 2005). SM is generated from the nonlinear interaction of ocean gravity waves of similar periods that are traveling in opposite directions (Longuet-Higgins, 1950; Ardhuin et al., 2011, 2015). In general, SM has relatively higher amplitudes as compared to that of PM in OBS stations.

The SM can be further classified into three types (class I to III) based on its origin (Ardhuin et al., 2011). Class-I SM is associated with a single storm, while class-II SM results from the superposition of ocean gravity wave with its coastal reflection. Class-III results from the interaction of swells arising from two distinct storms. Numerical modeling suggests that classes I and III are generated for body waves in the open ocean (Gerstoft et al., 2008; Zhang et al., 2010; Landès et al., 2010; Koper et al., 2010; Euler et al., 2014) and for Rayleigh waves (Cessaro, 1994; Stehly et al., 2006; Obrebski et al., 2012), whereas class II originates in near-shore regions (Chevrot et al., 2007; Bromirski et al. 2013). SM rarely propagate from deep oceans to the coastal areas (Bromirski et al., 2013; Ying et al., 2014); however, some researchers have contradicted this argument (Beucler et al., 2015; Tian and Ritzwoller, 2015; Gualtieri et al., 2015).

Microseism source characterization has wide applications in many fields such as earth and atmospheric sciences, oceanography, marine sciences, natural hazards, etc. Microseisms can be used to track storms propagating across ocean basins and to monitor ocean wave activity (Ebeling and Stein, 2011; Sun et al., 2013; Davy et al., 2014; Lin et al., 2014; Sheen, 2014; Sufri et al., 2014; Barruol et al., 2015; Xiao et al., 2018) and can supplement satellite and oceanographic observations particularly in regions of inadequate buoy data coverage. The other applications of microseisms are imaging the earth's interior using ambient noise tomography (Behr et al., 2010; 2011; Sabra et al., 2005; Shapiro et al., 2005; Gerstoft et al., 2006; Yang et al., 2007; Yao et al., 2008; Zhang et al., 2010) and making inferences about global climate change (Bromirski et al., 1999; Grevemeyer et al., 2000; Bromirski and

Duennebier, 2002; Aster et al., 2008; Stuzman et al., 2009). However, the method's accuracy and reliability are affected by the source regions of microseismic noises (Yao and van Der Hilst, 2009; Fichtner, 2014, 2015); therefore, a better understanding of microseism source distribution and propagation is required to explain the genesis of microseismic noise.

Numerous investigations have been carried out worldwide to understand microseismic noise (Aster et al., 2008; Gerstoft et al., 2008; Stutzmann et al., 2012). The noises in the Atlantic Ocean (Friedrich et al., 1998; Chevrot et al., 2007; Queiroz et al., 2017; Carvalho et al., 2019) and Pacific Ocean (Haubrich and McCamy 1969; Gerstoft and Tanimoto, 2007; Brooks et al., 2009; Koper et al., 2010; Behr et al., 2013) are well studied. Only a few studies are carried out in the South China Sea (Xiao et al., 2018) and the Southern Ocean (Reading et al., 2014). Likewise, the noises in the Indian Ocean are covered by relatively fewer studies (Koper and De Foy 2008; Sheen 2014; Davy et al., 2014, 2015; Rindraharisaona et al., 2020).

The intense storm activities in the South Indian Ocean generate ocean surface gravity waves that can propagate thousands of kilometers, circumscribing the hemisphere and reaching distant coasts as long-period waves or swells (Barber and Ursell, 1948; 1963; Snodgrass et al., 1966). For example, the North Indian Ocean region had reported on the modulation of local wind-waves at Kalpakkam, Tamil Nadu from remote forcing effects of Southern Ocean swells (Nayak et al., 2013). A multi-scale modeling approach was used to understand the role of distant swells and their impact on modifying and modulating the sea-state in the presence of locally generated wind-waves. They showed that swells from the Southern Ocean influence the local wind-waves in about four days time. In another study, Remya et al. (2015) reported the teleconnection between North Indian Ocean high swell events and meteorological conditions in the Southern Ocean using a combination of in situ measurements and model simulations. The Southern hemisphere has roaring forties, a strong westerly wind system located between latitudes 40 °S and 50 °S.

The local wind-wave climate of a region is also influenced by swells, which play an essential role in redistributing the energy of ocean waves (Nayak et al., 2013). Based on ocean wave spectral analysis, initial studies on the propagation of swells for major ocean basins are documented by Barber and Ursell (1948). Alves (2006) investigated ocean swells' contribution to the global wind-wave climate and postulated that swells that originate in the Southern Ocean contribute a major portion of wave energy to the global oceans. Low-frequency swells can also lead to coastal flooding (Kurian et al., 2009). Further, the influence of distant swells that propagate from the South Indian Ocean on the local wind-wave climate during cyclone *Phailin* was reported by Sandhya et al. (2015) and Remya et al. (2016).

CSIR-national institute of oceanography carried out a passive seismic experiment in the Andaman and Nicobar region, Bay of Bengal (Dewangan et al., 2017; Singha et al., 2018). This dataset gave us a unique opportunity to study microseismic noise in the Indian Ocean and understand their genesis. We analyzed the spatial and temporal variations of microseismic noise and attempt to establish a linkage between microseisms and ocean wave parameters in the Andaman-Nicobar region (Fig. 1). Such correlation helps in mapping the source region of microseismic noise worldwide (Tindle and Murphy, 1999; Bromirski, 2001; Rhie and Romanowicz, 2006; Zhang et al., 2009; Chen et al., 2011). We demonstrate that the swells originating in the South Indian Ocean have a possible linkage with microseisms in the Northern Indian Ocean.

Data and methodology

Seismological Data

Nine ocean-bottom seismometers (OBSs) data (Dewangan et al., 2017) and three ISLAND stations (HUTB, PBA and BARA) data (Srijayanti et al., 2012) from the Andaman and Nicobar region and six continental stations (PMBI, PSI, LHMI SIM, MHIT, PKBT) were used to characterize microseismic noises in the Indian Ocean (Fig. 1). OBSs were deployed from January 2014 to May 2014 to understand the seismicity and tectonics of the Andaman-Nicobar region (Dewangan et al., 2017; Singha et al., 2018). OBS was equipped with a Güralp CMG-40T seismometer (corner period of 60 s) and a broadband HTI-04-PCA/ULF hydrophone (100 s to 8 kHz). The orientations of OBSs were obtained from the analysis of Rayleigh waves (Dewangan et al., 2017) and are reliably estimated for only four stations (OBS02, OBS05, OBS09 and OBS11), which are used in the present study (Fig.1). The ISLAND/continental stations belong to the national center for ocean information services (INCOIS) (HUTB, BARA and PBA), Thai Seismic Monitoring Network (MHIT and PBKT), GEOFONE GE Seismic Network (LHMI and PMBI), GEOFONE IA Seismic Network (PSI) and Myanmar National Seismic Network (SIM).

Ocean wave model

ERA5 dataset is a fifth-generation of European Centre for Medium-Range Weather Forecasts (ECMWF) atmospheric reanalysis for the global climate. This dataset is an assimilated product obtained by ingesting model-derived data with observations for the global oceans. The ERA5 was produced using the 4D-Var (Four-Dimensional Variational Data Assimilation) data assimilation system of ECMWF Integrated Forecast System (IFS) comprising 137 hybrid sigma levels in the vertical. The top-most atmospheric level in ERA5 is prescribed at 0.01 hPa. Atmospheric data from the surface to the top-most level are interpolated to 37 pressure levels. Being an assimilated product using 4D-Var,

the researchers find that the data quality is superior and has potential applications for research use. ERA5 dataset is available for each hour of the day as a gridded product having global coverage. This data has a horizontal resolution of $0.25^{\circ} \times 0.25^{\circ}$ for the atmospheric variables, and $0.5^{\circ} \times 0.5^{\circ}$ for ocean waves. This datasets' availability covers a period starting from 1979 till present with a one-hour temporal resolution at each grid location. Here, we used the ERA5 dataset of ocean waves for the Indian Ocean domain (30°N – 70°S ; 30°E – 120°E) during January–April, 2014. This study analyzed several ocean wave parameters (Table 1) to establish their correlation with microseismic noise in the Andaman-Nicobar region. Various parameters analyzed are as follows: significant wave height (SWH), and its component due to wind-waves and total swells, combined wind-waves and swell, first/second/third swell partitions; mean wave period, and its component due to wind-waves and total swells, first/second/third swell partitions; mean wave direction, and its component due to total swells, first/second/third swell partitions. In ERA5, the swell wave system is addressed by partitioning the swell spectrum into three parts, and labeled as first, second, and third based on their respective wave heights. The spectral partitioning algorithm of Hanson and Phillips (2001) is used to decompose the swell spectrum into swell systems. The corresponding significant wave height, mean wave direction and period are computed based on the partitioned spectrum to differentiate swell wave systems produced from different sources.

The wave height data from ERA5 analysis has been critically validated against independent buoy observations (Hersbach et al., 2020). The validation exercise revealed that compared to ERA-Interim datasets, the performance of ERA5 was much better in terms of scatter index (normalized standard deviation). The scatter index based on validation against independent buoy wave heights is much lower in ERA5, demonstrating the improved data quality of ERA5 (Hersbach et al., 2020) used in the present study.

Polarization analysis

Numerous techniques exist for the analysis of microseismic noise like the cross-correlation (Landès et al., 2010; Tian and Ritzwoller, 2015), back projection (Ishii et al., 2005, 2007), a combination of cross-correlation with back projection (Shapiro et al., 2006; Stehly et al., 2006), beamforming (Cessaro, 1994; Gerstoft and Tanimoto, 2007; Euler et al., 2014; Gal et al., 2016;) and polarization techniques (Park et al., 1987; Schulte-Pelkum et al., 2004; Koper and Hawley, 2010; Schimmel et al., 2011). A major limitation of back projection, cross-correlation and beamforming methods is the requirement of multiple stations or dense networks. In contrast, the polarization method can be performed at a single station. Therefore, we used a frequency-dependent polarization approach (Schimmel and Gallart, 2003, 2004, 2005; Schimmel et al., 2011) to identify source regions. The three-component seismic data was

filtered for specific microseismic periods (1-5 s for SPDF, 6-10 s for LPDF and 11-20 s for PM) and converted to ground motion after accounting for instrument response. The processed data was divided into two-hour length segments, and each segment was transformed into the time-frequency domain using S-transform (Stockwell et al., 1996; Ventosa et al., 2008).

We obtained the degree of polarization (DOP) and the back azimuth as a function of time and frequency. The DOP is built from the semi-major and semi-minor axes of an ellipse that best fits the ground motion. The time-frequency variations of the semi-major and semi-minor axes are determined through eigenvalue analysis of three components seismogram. DOP (t, f) is expressed by a mean vector $\bar{m}(t, f)$ and planarity vector $\bar{p}(\tau, f)$ as,

$$DOP(t, f) = \left(\frac{1}{N(f)} \sum_{\tau=t-\frac{T(f)}{2}}^{\tau=t+\frac{T(f)}{2}} \left| \frac{\bar{m}(t, f)}{|\bar{m}(t, f)|} \cdot \frac{\bar{p}(\tau, f)}{|\bar{p}(\tau, f)|} \right|^{v_1} \right)^{v_2} \quad (\text{eq. 1})$$

$$\text{and } \bar{m}(t, f) = \frac{1}{N(f)} \sum_{\tau=t-\frac{T(f)}{2}}^{\tau=t+\frac{T(f)}{2}} \frac{\bar{p}(\tau, f)}{|\bar{p}(\tau, f)|} \quad (\text{eq. 2})$$

$\bar{p}(\tau, f)$ represents the cross product of semi-major and semi-minor vectors of the ellipse. For a linear or almost linear particle motion with linearity greater than 0.7, the planarity vector is replaced by the semi-major vector. We used a Gaussian window T(f) of length 17 s. In analogy to multiresolution analysis, the window size is scaled up/down by four times, which translates linearly with period of interest for stable results. N (f) is the number of samples in each window, and 100 samples are used in this study. v_1, v_2 are exponents used to control the number of polarized signals with DOP above the preset threshold of 0.7. Ambiguity regarding $\pm 180^\circ$ also is resolved by assuming retrograde elliptical ground motion of the Rayleigh wave.

Results and discussions

Double frequency microseisms in the Andaman-Nicobar regions

Microseismic noise levels are within the Peterson's noise limits for all OBSs located in the Andaman and Nicobar region (Dewangan et al., 2017). The amplitude spectra of microseisms (2 to 20 s) vary temporally and spatially for OBSs (Fig. 2) and continent stations (Fig. 3). In general, we observed splitting of double frequency microseisms into two or more peaks on all OBS and most of the LAND stations (Figs. 2,3). However, splitting is not observed on the inland stations (MHIT and PKBT) located far away from the coast. In the present study, we divided double frequency microseisms into SPDF (2-5 s) and LPDF (6-10 s). We observe that SPDF microseisms were strongest in January as

compared to that in April. In contrast, LPDF microseisms show an inverse relationship and were strongest in April. We strategically choose nine land stations to compare OBSs' noise levels with those from continental stations; 3 Island stations from Andaman and Nicobar Islands (HUTB, PBA and BARA), three stations from the Sumatra region (PMBI, PSI and LHMI), one coastal station (SIM) and two Inland stations from Thailand (PBKT and MHIT). It is interesting to observe that all continental stations except SIM, PBKT and MHIT show a similar temporal pattern for SPDF and LPDF microseisms, i.e., SPDF were strongest in January and LPDF were strongest in April.

Koper and Burlacu (2015) attributed the splitting of DF microseisms into SPDF and LPDF due to the interaction of noise signals generated from different regions. The Andaman-Nicobar region's local wind system is stronger in January and might explain the strongest SPDF microseisms during this period. In contrast, LPDF microseisms show an inverse pattern and were strongest in April. The wind system in the extra-tropical south Indian Ocean is strongest during June-October (Zieger et al., 2014). During the OBS deployment period (Jan-Apr), the winds in the South Indian Ocean were relatively stronger in April (Fig. 6); therefore, we infer that LPDF microseisms are related to distant sources in the South Indian Ocean.

Secondary microseisms (both SPDF and LPDF) show spatial variations in addition to temporal variations. Microseisms are weak for OBS06 and OBS07 located in deep waters (> 3500 m) and farthest from the coastline. However, other OBSs located in deep waters (OBS01, OBS03 and OBS12) show relatively higher SM noise, as they are closer to the coastline (Figs. 1,2). In general, OBSs located in shallower depths (< 2000 m) and in the proximity of coastline or seamounts (OBS05, OBS09, OBS11) exhibit strong microseismic noise. The only exception is OBS02, which is located in moderate water depth (1832 m) and is in the proximity to submarine volcanoes but show weak microseismic noise. These observations suggest that microseismic noises are more sensitive to coastlines/seamounts' proximity than to water depths in the Andaman and Nicobar region. Noise levels in Island stations (HUTB, PBA and BARA) are slightly lower than those from OBS stations. The continental stations (PMBI, PSI, LHMI and SIM) show even lower noise. The inland stations (PBKT and MHIT) exhibit the lowest noise level among all stations. These observations suggest that SM energy attenuates as they transition from deep water to shelf regions to continent.

The PM with a dominant period of 15 s was observed for all LAND stations (Fig. 3) and the shallowest OBS station (OBS11) and is not observed in other OBS stations located in deep waters (>1800 m). According to first-order theory, PM is the strongest microseismic noise in coastal regions due to the breaking of swells, but cannot effectively propagate to deep oceans as observed in the South China Sea (Xiao et al., 2018). As most OBS stations are located in deep waters, they do not show the dominant

peak associated with PM in the Andaman-Nicobar region. The absence of PM on OBSs might also indicate either source regions are far from OBS stations or are obscured by high noise levels at the ocean floor.

Polarization of microseisms in the Andaman-Nicobar region

A data matrix of polarized signals as a function of time, frequency, back azimuth at source and instantaneous degree of polarization is prepared for analysis. We selected signals with high degrees of polarization (> 0.7) and inferred microseisms' directional characteristics in the Andaman and Nicobar Islands. The polarized signals in the entire microseisms band (2-20s) are divided into SPDF (2-5s), LPDF (6-10s) and PM (11-20s) sub-bands. We selected only four OBS stations, whose horizontal orientations are reliable (OBS02, OBS05, OBS09 and OBS11 after Dewangan et al., 2017) and three LAND stations (PBA, BARA and PSI) for polarization analysis. We observe that strong local earthquakes and their aftershock sequence largely influence the polarization analysis; therefore, we manually identified and removed these large earthquake signals before polarization analysis.

The frequency-dependent polarization for the selected OBSs is shown in Figure 4 for the entire deployment period. The inner and outer circles of each sub-band represent 2 and 5 s for SPDF, 6 and 10 s for LPDF and 11 and 20 s for PM. The numbers of polarized signals are remarkably higher for SPDF as compared to LPDF and PM. The total number is largest in LPDF and PM bands for OBSs located over Alcock and Sewell seamounts (OBS05 and OBS09), situated over a thin sedimentary cover. The OBS11, located over accretionary prism with thick sediments, shows a fewer number of polarized signals. These observations suggest that microseisms, comprising of Love and Rayleigh waves, may propagate effectively in low sediment cover and get attenuated due to unusually low velocities of thick marine sediments. A strong polarized signal is observed in the PM band with dominant periods of 12, 14 and 16 s corresponding to the Rayleigh wave.

Dominant polarization directions for the SPDF band vary significantly among OBSs; however, they are remarkably consistent for LPDF and PM bands for an individual OBS. The signals are mostly oriented along northwest-southeast direction for OBS02 and OBS05 and northeast-southwest direction for OBS09 and OBS11. OBSs show two back azimuth directions for the LPDF band, which may be attributed to reflections of waves from the Andaman Islands and volcanic arc/seamounts. A similar polarization is observed in the Cape Verde archipelago in the Atlantic Ocean (Carvalho et al., 2019). Also, the variations in direction may be related to the uncertainty in the OBS orientation. The Andaman's bathymetry is quite complex, which might lead to changes in the signal propagation

direction. The monthly variation of polarization spectra also reveals similar polarization directions for all four months though the numbers of polarized signals vary (Figs. S1 to S4).

Back azimuths of elliptically polarized signals at BARA, PBA and PSI stations are shown in Figure 5. The number of polarized signals is remarkably high for PSI in all bands. Polarization plots for Island stations (BARA and PBA) are similar to OBS stations (Figs. 4 and 5). BARA demonstrates that SPDF is directed towards the east while LPDF and PM are directed towards the southwest. PBA shows multiple directions for SPDF, suggesting the sources are local while LPDF and PM direct towards west and southwest. PSI shows a consistent southwest direction for all bands. Monthly variations of polarization spectra for LAND stations are presented in Figures S5 to S7, and they show that polarization directions are consistent for the entire deployment period. It is interesting to note that LPDF and PM bands show consistent southwest directions for all OBS and continent stations, indicating that they originate from the same source in the South Indian Ocean. The analysis of OBS data from the Rhum-Rhum experiment (Davy et al., 2015) and land stations from La Reunion (Rindraharisaona et al., 2020) also suggests that the source region of microseisms lies in the South Indian Ocean. The absence of consistent direction for the SPDF band suggests local origin.

Linkages between microseisms and swells in the Andaman-Nicobar region

We studied several ocean wave parameters (Wind speed, significant wave height, mean wave period, mean wave direction, etc.) in the Andaman-Nicobar region to establish their linkages with microseismic noise in SPDF, LPDF, and PM bands. Spatio-temporal variations of 10-m wind speed and direction for the Indian Ocean region during the deployment period are shown in Figure 6. The western and eastern sectors of the extra-tropical South Indian Ocean (ETSIO) and Southern Ocean (SO) regions experience the highest wind speed exceeding 9 m s^{-1} , sometimes reaching about $13\text{-}15 \text{ m s}^{-1}$ (Figs. 6b-d). Typically, this region is persistent with very strong westerlies and generates swell waves that eventually propagate towards the North Indian Ocean (NIO) region (Kurian et al., 2009; Nayak et al., 2013; Zheng et al., 2018). The tropical south Indian Ocean (TSIO, 35° S : EQ; 30° E : 120° E) experiences moderate wind speed, with persistent strong easterlies (Figs. 6a-d). The tropical north Indian Ocean (TNIO) region comprises the Arabian Sea (EQ: 30° N ; 30° E : 78° E), Bay of Bengal (EQ: 30° N ; 78° E : 105° E), and South China Sea (SCS, EQ: 30° N ; 105° E : 120° E). Winds are relatively stronger in the SCS region (Figs. 6a-b) during January and February ranging between $9\text{-}15 \text{ m s}^{-1}$, and a part of this system enters the Andaman Sea through the Gulf of Thailand and Malacca Strait. Interaction of local waves generated due to strong wind in the Andaman region during January may explain high SPDF microseismic noise during this period. During March and April, the transitions

in winds' speed are noticed over the head Bay of Bengal region (Figs. 6c-d), and the wind speed is relatively low, which may explain low SPDF microseismic noise in April.

Monthly averaged significant wave heights for the Indian Ocean region during January-April are shown in Figure 7. The southern sector of TSIO and SO experiences the highest significant wave heights exceeding 4.0 m, especially during February-April (Figs 7b-d). Monthly mean wave heights range from 1.0 to 1.5 m in the Bay of Bengal. Regions in the SCS experience relatively higher wave heights in the order of 2.0-2.5 m during January-February (Figs. 7a-b). Wave heights decrease during March-April due to the weakening of the wind system in the transition period. In general, based on the orientation of wave height contours, the significant wave heights are seen increasing from the southern to the northern hemisphere, indicating the presence and dominance of distant swells generated from the SO and their role in influencing the local wind-wave climate of NIO. Monthly averaged wave periods and wave direction are shown in Figures S8 and S9, respectively. The swell-generating area in the SO has the highest mean wave period exceeding 9.0 s during January-April. Regions in the western TSIO experience wave period of 7.5 s, whereas the eastern sector has relatively higher mean wave periods in the order of 9.0 s. In general, the mean wave periods in the SO are higher during March-April as compared to January-February. Eastern sectors in the SO belt show a mean wave period of 10.5 s during April that is directly linked to strengthening of winds over this region (Figure 6d). Strengthening of winds in the SO (Figs. 6c-d) is directly related to higher significant wave heights (Figs. 7c-d) and a higher mean wave period (Figs. S8c-d). It is notable that with increasing wave activity in the SO sector, the mean wave period in the NIO is also found increasing, and that is more prominent over the Bay of Bengal as compared to the Arabian Sea. The mean wave direction ($\sim 270^\circ$) over the SO (Fig. S9) belt lie almost aligned with the wind direction of the strong westerlies (Fig. 6). It is seen that for the southern belt in the TSIO, the mean wave direction is aligned towards the southerly wave propagation direction ($\sim 180^\circ$). It deciphers the propagation and dispersion of wave energy from the SO belt migrating towards the Northern hemisphere centered in the southerly and south-easterly directions. Propagation of wave energy from the southerly and south-westerly directions is evident in the eastern sector of the TSIO belt. During March-April, the mean wave direction is oriented southerly and south-westerly in the TNIO, influencing the wind-wave climate in regions over the Bay of Bengal.

Daily records of microseismic noise for SPDF, LPDF, PM bands were extracted for all OBSs and two island stations (BARA and PBA) to evaluate the linkages between noise in the Andaman-Nicobar region and ocean wave parameters. Likewise, daily records of relevant ocean wave parameters such as significant wave heights, mean wave period and mean wave directions were extracted at each location

from the ERA5 dataset. Time series distribution of 120 days (OBS's deployment period) for microseismic noise and ocean wave parameters is shown for a representative OBS (Fig. 8). The Pearson correlation coefficient (R) was calculated as a statistical correlation between OBS/island stations and ocean wave parameters and is listed in Table 1 for SPDF, LPDF and PM bands. We observed large positive correlations (0.63 - 0.81) between wind speed / significant height of wind waves and SPDF, indicating the role of wind-induced local waves towards the genesis of SPDF microseisms for OBS/island stations.

We analyzed the correlations of SPDF with significant heights corresponding to swell/wind-waves, first and second swell partitions, and observed that they are largest for wind-waves for OBS. Large negative correlations (-0.67 to -0.81) are observed between mean wave period and SPDF, indicating that short-period (high-frequency) waves generate stronger SPDF microseisms than long-period waves. The mean wave directions (70-250°) show negative correlations (-0.44 to -0.76) with SPDF noise, suggesting that wave directions (70-100°), perpendicular to coastlines, generate stronger SPDF.

In contrast, moderate negative correlations (-0.17 to -0.40) are observed between wind speed and LPDF noise for all OBSs except OBS12. Poor correlations (-0.29 to 0.27) are observed between SWH and LPDF, indicating that local wind-induced waves do not significantly impact the generation of LPDF microseisms. Moderate positive correlations (0.37 – 0.65) are observed between mean wave period/mean period of total swells and LPDF for most OBSs and island stations, indicating that long-period (low-frequency) waves generate the strongest LPDF microseisms. We presume that long-period waves travel from long distances; therefore, the source region of LPDF microseisms is far from the Andaman Islands. The mean wave directions for most OBSs show moderate positive correlations (0.27-0.53) with LPDF noise, suggesting that wave direction (170-200°), pointing towards the South Indian Ocean, generate stronger LPDF.

Poor correlations are also observed between amplitudes of PM (11–20 s) and SWH for most OBSs and island stations, indicating that SWH may not govern the PM (Table 1). Rindraharisaona et al. (2020) characterized microseismic noise at La Reunion Island in the western Indian Ocean. They observed a high correlation between SWH and PM, indicating that PM can be used as a proxy for swell height. We do not detect a similar phenomenon for the marginal Andaman Sea as the lack of PM signal on OBSs does not permit such analysis.

Summary and conclusions

We analyzed the microseismic noise and attempted to understand its genesis in the Andaman-Nicobar region, Bay of Bengal. We observed double frequency microseisms splitting into SPDF (2 – 5 s) and

LPDF (6 – 10 s) on OBS and continental stations. The SPDF microseisms show a strong dependence on local wind conditions and geomorphology and were strongest in January when wind speeds are higher. They are randomly polarized and show a strong correlation with the significant height of wind waves. They are excited by short-period waves that are perpendicular to the Andaman-Nicobar Islands. In contrast, LPDF microseisms show consistent polarization, which points towards the South Indian Ocean. The amplitude of LPDF was strongest in April when the gusty winds exist in roaring forties and furious fifty in the southern Indian Ocean. They are excited by long-period waves oriented in north-south directions.

Data and resources

The ocean-bottom seismometer (OBS) data were acquired in the Andaman–Nicobar region under the Council of Scientific and Industrial Research - Geodynamics and Earthquake generating processes in NE India and Andaman Subduction zone (CSIR-GENIAS) Project. The waveform data for the BARA station were provided by Earth System Sciences Organization - Indian National Centre for Ocean Information Services (ESSO-INCOIS), Ministry of Earth Sciences, Government of India on 22nd August 2016. Earthquake data for the continental stations were compiled from the IRIS Data Management Center (IRIS DMC). The monitoring network comprises of Thai Seismic Monitoring Network (MHIT and PBKT), GEOFONE GE Seismic Network (LHMI and PMBI), GEOFONE IA Seismic Network (PSI), Malaysian National Seismic Network (KUM) and Myanmar National Seismic Network (SIM). All the figures are made using MATLAB R2019b. M-Map toolbox was used for plotting (Pawlowicz, 2020). Polfre code was used for the polarization analysis. The figures (Figs. S1-S9) are provided as supplementary material.

Acknowledgments

We would like to thank the Director, CSIR- NIO for supporting the study. We would like to thank the Director, ESSO-INCOIS for providing the BARA data. Earthquake data for the LAND stations were compiled from the International Seismological Centre (ISC). We thank the anonymous reviewers and associate editor for comments/suggestions, which have improved the manuscript's quality. The author R. Reddy acknowledges the science and education research board (SERB) for a national postdoctoral fellowship (NPDF) at CSIR-NIO, where OBS data processing data was carried out. The author R. Reddy also acknowledges IIT Kharagpur for the institute's postdoctoral fellowship. We thank Dr. Martin Schimmel for providing the polfre code. This is CSIR-NIO contribution no. xxx.

References

- Alves, J. H. G. M. (2006). Numerical modelling of ocean swell contributions to the global wind-wave climate, *Ocean Modelling*. **11(1-2)**, 98–122.
- Ardhuin, F., E. Stutzmann, M. Schimmel, and A. Mangeney (2011). Ocean wave sources of seismic noise, *J. Geophys. Res.* **116**, no. C09004, doi:10.1029/2011JC006952.
- Ardhuin, F., L. Gualtieri, and E. Stutzmann (2015). How ocean waves rock the Earth: Two mechanisms explain microseisms with periods 3 to 300s, *Geophys. Res. Lett.* **42**, no. 3, 765–772.
- Aster, R.C., D.E. McNamara, and P.D. Bromirski (2008). Multidecadal climate-induced variability in microseisms, *Seism. Res. Lett.* **79(2)**, 194–202.
- Barber, N. F., and F. Ursell (1948). The generation and propagation of ocean waves and swell. Part I. Wave periods and velocities. *Philos. Trans. Royal Soc. London A*, **240**, 527–560.
- Barruol, G., C. Davy, F. R. Fontaine, V. Schlindwein, and K. Sigloch (2015). Monitoring austral and cyclonic swells in the "Iles Eparses" (Mozambique channel) from microseismic noise, *Acta Oecol.* **72**, 120–128.
- Behr, Y., J. Townend, S. Bannister, and M.K. Savage (2010). Shear velocity structure of the Northland Peninsula, New Zealand, inferred from ambient noise correlations. *Journal of Geophysical Research*, **115**, B05309.
- Behr, Y., J. Townend, S. Bannister, and M.K. Savage (2011). Crustal shear wave tomography of the Taupo volcanic zone, New Zealand, via ambient noise correlation between multiple three-component networks, *Geochemistry, Geophysics, Geosystems*, **12**, Q03015. <https://doi.org/10.1029/2010GC003385>
- Behr, Y., J. Townend, M. Bowen, L. Carter, R. Gorman, L. Brooks, and S. Bannister (2013). Source directionality of ambient seismic noise inferred from three-component beamforming, *J. geophys. Res.* **118**, 240–248.
- Beucler, É., A. Mocquet, M. Schimmel, S. Chevrot, O. Quillard, J. Vergne, and M. Sylvander (2015). Observation of deep water microseisms in the North Atlantic Ocean using tide modulations, *Geophys. Res. Lett.* **42**, no. 2, 316–322.
- Bromirski, P. D. (2001). Vibrations from the "Perfect Storm", *Geochemistry, Geophysics, Geosystems*. **2**, 1030. <https://doi.org/10.1029/2000GC000119>
- Bromirski, P. D. (2009). Earth vibrations, *Science*. **324**, 1026.
- Bromirski, P. D., R. A. Stephen, and P. Gerstoft (2013). Are deep-oceangenerated surface-wave microseisms observed on land?, *J. Geophys. Res.* **118**, no. 7, 3610–3629, doi: 10.1002/jgrb.50268.
- Bromirski, P. D and F.K. Duennebieer (2002). The near-coastal microseism spectrum: Spatial and temporal wave climate relationships, *Journal of Geophysical Research*. **107(B8)**, 2166.
- Bromirski, P. D., F. K. Duennebieer, and R. A. Stephen (2005). Mid-ocean microseisms, *Geochem. Geophys. Geosys.* **6**, no. 4, doi: 10.1029/2004GC000768.

- Bromirski, P.D., R.E. Flick, and N. Graham (1999) Ocean wave height determined from inland seismometer data: Implications for investigating wave climate changes in the NE Pacific, *Journal of Geophysical Research*. **104**, 20,753–20,766. <https://doi.org/10.1029/1999JC900156>
- Brooks, L.A., J. Townend, P. Gerstoft, S. Bannister, and L. Carter (2009). Fundamental and higher-mode Rayleigh wave characteristics of ambient seismic noise in New Zealand, *Geophys. Res. Lett.*, **36**, doi:10.1029/2009GL040434.
- Carvalho, J.F., G.Silveira, M. Schimmel, and E. Stutzmann (2019). Characterization of Microseismic Noise in Cape Verde. *Bulletin of the Seismological Society of America*, 109(3), pp.1099-1109.
- Cessaro, R., (1994). Sources of primary and secondary microseisms, *Bull. Seismol. Soc. Am.* 84, 142–148.
- Chen, Y.-N., Y. Gung, S.-H. You, S.-H. Hung, L.-Y. Chiao, T.-Y. Huang, et al. (2011). Characteristics of short period secondary microseisms (SPSM) in Taiwan: The influence of shallow ocean strait on SPSM, *Geophysical Research Letters*. **38**, L04305. <https://doi.org/10.1029/2010GL046290>
- Chevrot, S., M. Sylvander, S. Benahmed, C. Ponsolles, J.M.Lefèvre, and D. Paradis (2007). Source locations of secondary microseisms in western Europe: Evidence for both coastal and pelagic sources, *J. Geophys. Res.* **112**, 1–19.
- Curry, J. R (2005). Tectonics and history of the Andaman Sea region, *J. Asian Earth Sci.* **25**, 187–232
- Davy, C., E.Stutzmann, G. Barruol, F.R. Fontaine, and M. Schimmel (2015). Sources of secondary microseisms in the Indian Ocean, *Geophys.J. Int.* **202**, 1180–1189.
- Davy, C., G. Barruol, F. R. Fontaine, K. Sigloch, and E. Stutzmann (2014). Tracking major storms from microseismic and hydroacoustic observations on the seafloor, *Geophys. Res. Lett.* **41**, no. 24, 8825–8831, doi: 10.1002/2014gl062319.
- Dee, D. P., S.M. Uppala, A.J. Simmons, P. Berrisford, P. Poli, S. Kobayashi, and P. Bechtold (2011). The ERA-Interim reanalysis: Configuration and performance of the data assimilation system, *Q. J. R. Meteorolog. Soc.* **137**, no. 656, 553-597
- Dewangan, P., R. Reddy, K. A. Kamesh Raju, P. Singha, K. K. Aswini, V. Yatheesh, K. Samudrala, and M. Shuhail (2017). Nature of the ambient noise, site response, and orientation of ocean-bottom seismometers (OBSs): Scientific results of a passive seismic experiment in the Andaman Sea, *Bull. Seismol. Soc. Am.* **108**, no. 1, 248–259, doi: 10.1785/0120170163.
- Ebeling, C. W., and S. Stein (2011). Seismological identification and characterization of a large hurricane, *Bull. Seismol. Soc. Am.* **101(1)**, 399–403.
- Euler, G. G., D. A. Wiens, and A. A. Nyblade (2014). Evidence for bathymetric control on the distribution of body wave microseism sources from temporary seismic arrays in Africa, *Geophys. J. Int.* **197**, no. 3, 1869–1883.
- Fichtner, A. (2014). Source and processing effects on noise correlations, *Geophys. J. Int.* **197**, no. 3, 1527–1531, doi: 10.1093/gji/ggu093.
- Fichtner, A. (2015). Source-structure trade-offs in ambient noise correlations, *Geophys. J. Int.* **202**, no. 1, 678–694, doi: 10.1093/gji/ggv182.

- Friedrich, A., F. Kruger, and K. Klinge (1998). Ocean-generated microseismic noise located with the Grafenberg array, *J. Seismol.* **2**(1), 47–64.
- Gal, M., A. Reading, S. Ellingsen, K.D. Koper, R. Burlacu, and S. Gibbons (2016). Deconvolution enhanced direction of arrival estimation using one- and three-component seismic arrays applied to ocean induced microseisms, *Geophys. J. Int.* **206**, 345–359.
- Gerstoft, P., and T. Tanimoto (2007). A year of microseisms in southern California, *Geophys. Res. Lett.* **34**, L20304, doi:10.1029/2007gl031091.
- Gerstoft, P., K.G. Sabra, P. Roux, W.A. Kuperman, and M.C. Fehler (2006). Green's functions extraction and surface-wave tomography from microseisms in southern California, *Geophysics.* **71**(4), SI23–SI31.
- Gerstoft, P., P. Shearer, N. Harmon, and J. Zhang (2008). Global P, PP, and PKP wave microseisms observed from distant storms, *Geophys. Res. Lett.* **35**, doi:10.1029/2008GL036111.
- Gupta, N., Prasad K. Bhaskaran, Mihir K. Dash (2015). Recent Trends in Wind-Wave Climate for the Indian Ocean, *Current science.* **108**(12), 2191-2201.
- Hasselmann, K., (1963). A statistical analysis of the generation of microseisms, *Reviews of Geophysics.* **1**, 177–210. <https://doi.org/10.1029/RG001i002p00177>
- Haubrich, R.A., and K. McCamy (1969). Microseisms: coastal and pelagic sources, *Rev. Geophys.* **7**, 539–571.
- Havskov, J., and L. Ottemöller (2009). Introduction to SEISAN and Computer exercises in processing earthquake data.
- Hersbach, H., Bell, B., Berrisford, P., Hirahara, S., Horányi, A., Muñoz-Sabater, J., Nicolas, J., Peubey, C., Radu, R., Schepers, D., Simmons, A., Soci, C., Abdalla, S., Abellan, X., Balsamo, G., Bechtold, P., Biavati, G., Bidlot, J., Bonavita, M., De Chiara, G., Dahlgren, P., Dee, D., Diamantakis, M., Dragani, R., Flemming, J., Forbes, R., Fuentes, M., Geer, A., Haimberger, L., Healy, S., Hogan, R.J., Hólm, E., Janisková, M., Keeley, S., Laloyaux, P., Lopez, P., Lupu, C., Radnoti, G., de Rosnay, P., Rozum, I., Vamborg, F., Villaume, S., Thépaut, J.-N. (2020). The ERA5 global reanalysis. *Quarterly Journal of the Royal Meteorological Society*, <https://doi.org/10.1002/qj.3803>
- Hoffmann, L., G. Günther, D. Li, O. Stein, X. Wu, S. Griessbach, Y. Heng, P. Konopka, R. Müller, B. Vogel, and J.S. Wright (2019). From ERA-Interim to ERA5: The considerable impact of ECMWF's next-generation reanalysis on Lagrangian transport simulations, *Atmospheric Chemistry and Physics.* <https://doi.org/10.5194/acp-19-3097-2019>.
- Kamesh Raju, K. A., T. Ramprasad, P. S. Rao, B. R. Rao, and J. Varghese (2004). New insights into the tectonic evolution of the Andaman basin, northeast Indian Ocean, *Earth Planet Sci. Lett.* **221**, no.1, 145–162.
- Kamesh Raju, K. A., D. Ray, A. Mudholkar, G. P. S. Murty, V. K. Gahalaut, K. Samudrala, A. L. Paropkari, R. Ramachandran, and L. Surya Prakash (2012). Tectonic and volcanic implications of a cratered seamount off Nicobar Island, Andaman Sea. *Journal of Asian Earth Sciences*, **56**, 42-53. doi: 10.1016/j.jseaes.2012.04.018.

- Koper, K. D., and V.L. Hawley (2010). Frequency dependent polarization analysis of ambient seismic noise recorded at a broadband seismometer in the central United States, *Earthquake Science*. **23(5)**, 439–447.
- Koper, K.D., and B. De Foy (2008). Seasonal Anisotropy in Short-Period Seismic Noise Recorded in South Asia, *Bull. seism. Soc. Am.*, **98(6)**,3033–3045.
- Koper, K.D., K. Seats, and H. Benz (2010). On the composition of Earth’s short-period seismic noise field, *Bull. seism. Soc. Am.*, **100(2)**, 606–617.
- Kurian, N. P., N. Nirupama, M. Baba, and K.V. Thomas (2009). Coastal flooding due to synoptic scale, meso-scale and remote forcings, *Natural Hazards*,**48**, 259–273.
- Landès, M., F. Hubans, N.M. Shapiro, A. Paul, and M. Campillo (2010). Origin of deep ocean microseisms by using teleseismic body waves. *J.Geophys. Res.***115**, B05302.
- Lin, J. Y., T. C. Lee, H. S. Hsieh, Y. F. Chen, Y. C. Lin, H. H. Lee, and Y. Y. Wen (2014). A Study of microseisms induced by typhoon Nanmadol using ocean-bottom seismometers, *Bull. Seismol. Soc. Am.* **104**, no. 5, 2412–2421, doi: 10.1785/0120130237.
- Longuet-Higgins, M. S., (1950). A theory of the origin of microseisms, *Phil.Trans. Roy. Soc. Lond. A* **243**, no. 857, 1–35.
- McNamara, D. E., and R. Buland (2004). Ambient Noise Levels in the Continental United States, *Bull. Seismol. Soc. Am.***94**, no.4, 1517– 1527.
- Munk, W. H., G. R., Miller, F. E. Snodgrass, and N. F. Barber (1963). Directional recording of swell from distant storms, *Philos. Trans. Royal Soc. London A*, **255**, 5052584.
- Nayak, S., P. K. Bhaskaran, R. Venkatesan, and S. Dasgupta (2013). Modulation of local wind-waves at Kalpakkam from remote forcing effects of Southern Ocean swells. *Ocean Eng.*, **64**, 23–35.
- Obrebski, M. J., F. Ardhuin, E. Stutzmann, and M. Schimmel (2012). How moderate sea states can generate loud seismic noise in the deep ocean, *Geophys. Res. Lett.*, 39, L11601, doi:10.1029/2012GL051896.
- Pawlowicz, R., (2020). "M_Map: A mapping package for MATLAB", version 1.4m, [Computer software], available online at www.eoas.ubc.ca/~rich/map.html.
- Park, J., F.L. Vernon, and C.R. Lindberg (1987). Frequency dependent polarization analysis of high-frequency seismograms, *Journal of Geophysical Research*,**92**, 12,664–12,674.
- de Queiroz, D. É., A.F. do Nascimento, and M.Schimmel (2017). Microseismic noise in the Saint Peter and Saint Paul Archipelago, equatorial Atlantic. *Journal of South American Earth Sciences*, **80**, 304–315.
- Reading, A.M., K.D. Koper, M. Gal, L.S. Graham, H. Tkalčić, and M.A. Hemer (2014). Dominant seismic noise sources in the Southern Ocean and West Pacific, 2000–2012, recorded at the Warramunga Seismic Array, *Geophys. Res. Lett.*, **41**, 3455–3463.
- Remya, P. G., R. Kumar, S. Basu, and A. Sarkar (2012). Wave hindcast experiments in the Indian Ocean using MIKE 21 SW model, *J. Earth Syst. Sci.*, **121**, 385–392.

- Remya, P. G., S. Vishnu, B. Praveen Kumar, T.M. Balakrishnan Nair and B. Rohith (2016). Teleconnection between the North Indian Ocean high swell events and meteorological conditions over the Southern Indian Ocean, *Journal of Geophysical Research: Oceans*, **121**, 7476-7494, doi:10.1002/2016JC011723
- Rhie, J., and B. Romanowicz (2006). A study of the relation between ocean storms and the Earth's hum, *Geochemistry, Geophysics, Geosystems*.**7**, Q10004.
- Rindraharisaona, E.J., E Cordier, G Barruol, F R Fontaine, M Singh (2020). Assessing swells in La Réunion Island from terrestrial seismic observations, oceanographic records and offshore wave models, *Geophysical Journal International*. **221 (3)**, Pages 1883–1895.
- Sabra, K.G., P. Gerstoft, P. Roux, W.A. Kuperman, and M.C. Fehler (2005). Surface wave tomography from microseisms in Southern California, *Geophysical Research Letters*. **32**, L14311.
- Sandhya, K. G., P.G. Remya, T.M. Balakrishnan Nair, and N. Arun (2015). On the co-existence of high-energy low-frequency waves and locally-generated cyclone waves off the Indian east coast, *Ocean Eng.*, **111**, 148–154.
- Schimmel, M., and J. Gallart (2003). The use of instantaneous polarization attributes for seismic signal detection and image enhancement, *Geophys. J. Int.*, **155(2)**, 653–668.
- Schimmel, M., and J. Gallart (2004). Degree of polarization filter for frequency- dependent signal enhancement through noise suppression, *Bull. seism.Soc. Am.*, **94(3)**, 1016–1035.
- Schimmel, M., and J. Gallart (2005). The inverse S transform in filters with time-frequency localization, *IEEE Trans. Signal Process.*, **53(11)**, 4417–4422.
- Schimmel, M., E. Stutzmann, F. Ardhuin, and J. Gallart (2011). Polarized Earth's ambient microseismic noise, *Geochem. Geophys. Geosyst.* **12**, Q07014.
- Schulte-Pelkum, V., P.S.Earle, and F.L.Vernon (2004). Strong directivity of ocean-generated seismic noise, *Geochem. Geophys. Geosyst.* **5**, 1– 13.
- Shapiro, N. M., M. Campillo, L. Stehly, and M.H. Ritzwoller (2005). High-resolution surface-wave tomography from ambient seismic noise, *Science*, **307(5715)**, 1615–1618.
- Sheen, D.H., (2014). Microseisms from huge Indian Ocean storms in May 2007, *Geosci. J.*, **18(3)**, 347–354.
- Singh, S. C., and R. Moeremans (2017). Chapter 13 Anatomy of the Andaman–Nicobar subduction system from seismic reflection data, *Geol. Soc. Lond. Mem.* **47**, 193–204.
- Singha, P., P. Dewangan, K. A. Kamesh Raju, K. K. Aswini, and T. R. Reddy (2019). Geometry of the subducting Indian plate and local seismicity in the Andaman region from the passive OBS experiment, *Bull. Seismol. Soc. Am.* **109**, no. 2, 797–811.
- Snodgrass, F. E., G. W Groves, K. Hasselmann, G. R. Miller, W.H. Munk, and W.H. Powers (1966). Propagation of ocean swell across the Pacific, *Philos. Trans. Royal Soc. London, A*, **249**, 431–497.

- Srijayanthi, G., M. Ravi Kumar, T. Sirisha, K. Sushini, G. Srihari Prasad, P. Solomon Raju, Arun Singh, N. Purnachandra Rao (2012). The ISLANDS Network in the Andaman–Nicobar Subduction Zone, *Seismological Research Letters*. **83** (4), 686–696.
- Stehly, L., M. Campillo, and N.M. Shapiro (2006). A study of the seismic noise from its long-range correlation properties, *J. Geophys. Res.* **111**, 1–12.
- Stephen, R. A., F. N. Spiess, J. A. Collins, J. A. Hildebrand, J. A. Orcutt, K. R. Peal, F. L. Vernon, and F. B. Wooding (2003), Ocean Seismic Network Pilot Experiment, *Geochem. Geophys. Geosyst.*, 4(10), 1092, doi:10.1029/2002GC000485.
- Stockwell, R.G. (1996). Localization of the complex spectrum: The S transform, *IEEE Trans. Signal Process.*, **44**(4), 998–1001
- Stutzmann, E., F. Ardhuin, M. Schimmel, A. Mangeney, and G. Patau (2012). Modelling long-term seismic noise in various environments, *Geophys. J. Int.* **191**(2), 707–722.
- Sufri, O., K. D. Koper, R. Burlacu, and B. De Foy (2014). Microseisms from Superstorm Sandy, *Earth Planet. Sci. Lett.* **402**, 324–336, doi: 10.1016/j.epsl.2013.10.015.
- Sun, T., M. Xue, K. P. Le, Y. Zhang, and H. Xu (2013). Signatures of ocean storms on seismic records in South China Sea and East China Sea, *Mar. Geophys. Res.* **34**, nos. 3/4, 431–448, doi: 10.1007/s11001-013-9204-6.
- Tian, Y., and M.H. Ritzwoller (2015). Directionality of ambient noise on the Juan de Fuca plate: Implications for source locations of the primary and secondary microseisms, *Geophys. J. Int.* **201**, 429–443.
- Tindle, C.T., and M.J. Murphy (1999). Microseisms and ocean wave measurements, *IEEE Journal of Oceanic Engineering*, **24**(1), 112–115 <https://doi.org/10.1109/48.740159>
- Tolman, H. L., (1991). A third-generation model for wind waves on slowly varying, unsteady and inhomogeneous depths and currents, *J. Phys. Oceanogr.* **21**, no.6, 782–797.
- Ventosa, S., C. Simon, M. Schimmel, J.J. Dañobeitia, and A. Manuel (2008). S-transform from a wavelets point of view, *IEEE Trans. Signal Process.* **56**, 2771–2780.
- Xiao, H., M. Xue, T. Yang, C. Liu, Q. Hua, S. Xia, *et al.* (2018). The characteristics of microseisms in South China Sea: Results from a combined data set of OBSs, broadband land seismic stations, and a global wave height model, *Journal of Geophysical Research: Solid Earth*, **123**. <https://doi.org/10.1029/2017JB015291>
- Yang, Y., M.H. Ritzwoller, A.L. Levshin, and N.M. Shapiro (2007). Ambient noise Rayleigh wave tomography across Europe, *Geophysical Journal International*, **168**(1), 259–274.
- Yao, H., and R. D. Van Der Hilst (2009). Analysis of ambient noise energy distribution and phase velocity bias in ambient noise tomography, with application to SE Tibet, *Geophys. J. Int.* **179**, no. 2, 1113–1132, doi: 10.1111/j.1365-246X.2009.04329.x
- Yao, H., C. Beghein, and R.D. van der Hilst (2008). Surface wave array tomography in SE Tibet from ambient seismic noise and two-station analysis - II. Crustal and upper-mantle structure, *Geophysical Journal International*. **173**(1), 205–219. <https://doi.org/10.1111/j.1365-246X.2007.03696.x>

Ying, Y., C. J. Bean, and P. D. Bromirski (2014). Propagation of microseisms from the deep ocean to land, *Geophys. Res. Lett.* **41**, no. 18, 6374–6379, doi: 10.1002/2014gl060979.

Zhang, J., P. Gerstoft, and P.M. Shearer (2009). High-frequency P-wave seismic noise driven by ocean winds, *Geophysical Research Letters*.**36**, L09302.

Zhang, J., P. Gerstoft, and P.M. Shearer (2010). Resolving P-wave travel-time anomalies using seismic array observations of oceanic storms, *Earth and Planetary Science Letters*. **292(3–4)**, 419–427.

Zhang, J., P. Gerstoft, and P. D. Bromirski (2010). Pelagic and coastal sources of P-wave microseisms: Generation under tropical cyclones, *Geophys. Res. Lett.* **37**, L15301, doi: 10.1029/2010gl044288.

Zieger, S., Babanin, A.V., Young, I.R. (2014). Changes in ocean surface wind with a focus on trends in regional and monthly mean values. Deep Sea Research Part I: Oceanographic Research Papers, 86, 56-67.

Full mailing address for each author

Ramakrushna Reddy. T (Postdoctoral Fellow)
Former address: CSIR-National Institute of Oceanography (NIO)
Geological Oceanography Division
Goa
Present address: IIT Kharagpur
Dept of Geology and Geophysics
Email: rukisna@gmail.com

Pawan Dewangan (Principal Scientist)
CSIR-National Institute of Oceanography (NIO)
Geological Oceanography Division
Goa
Email: pdewangan@nio.org

Prasad Kumar Bhaskaran (Professor)
IIT Kharagpur
Dept of Ocean Engineering and Naval Architecture
Email: prasad.bhaskaran@gmail.com

Paresh Nath Singha Roy (Professor)
IIT Kharagpur
Dept of Geology and Geophysics
Email: pareshsr@gg.iitkgp.ac.in

List of figure captions

Figure 1: Location map of the study area. Stars are OBS stations and triangles are land stations. Zoom out of the study location is shown in the inset.

Figure 2: Monthly variation of microseism amplitude spectra for OBSs. Amplitudes are extracted from the vertical component. Legends show amplitudes for Jan to April, and they are same for all the subplots. D represents depth in meters.

Figure 3: Monthly variation of microseism amplitude spectra for continent stations. Amplitudes represent the vertical component. Legends show amplitudes for Jan to April, and they are same for all the subplots.

Figure 4: Polarization spectra for OBSs. Measurements represent the entire duration of OBS deployment. The color scale represents the number of polarized signals. As seen in LPDF and PM plots, the number of polarized signals is high only for certain periods i.e., the periods/frequencies corresponding to the Rayleigh waves at that station.

Figure 5: Polarization spectra for selected continental stations. Measurements represent the entire duration of OBS deployment. The color scale represents the number of polarized signals. As seen in LPDF and PM plots, the number of polarized signals is high only for certain periods i.e., the periods/frequencies corresponding to the Rayleigh waves at that station.

Figure 6: Monthly averaged 10m wind Speed and direction extracted from the ERA-5 dataset.

Figure 7: Monthly averaged significant wave heights extracted from the ERA-5 dataset.

Figure 8: Representative correlation of microseism (solid lines) with ocean wave parameters at OBS01. (a) SPDF Vs. SWH (b) SPDF Vs. wind speed (c) SPDF Vs. mean period (d) LPDF Vs. mean period.

List of table captions

Table 1: Correlation coefficient of microseismic noise in SPDF, LPDF and PM bands with wave parameters extracted from the ERA-5 dataset. Strong correlations (> 0.45) are marked in red, moderate correlations ($0.25-0.45$) are marked in green and poor correlations (< 0.25) are marked in black.

Figure 1

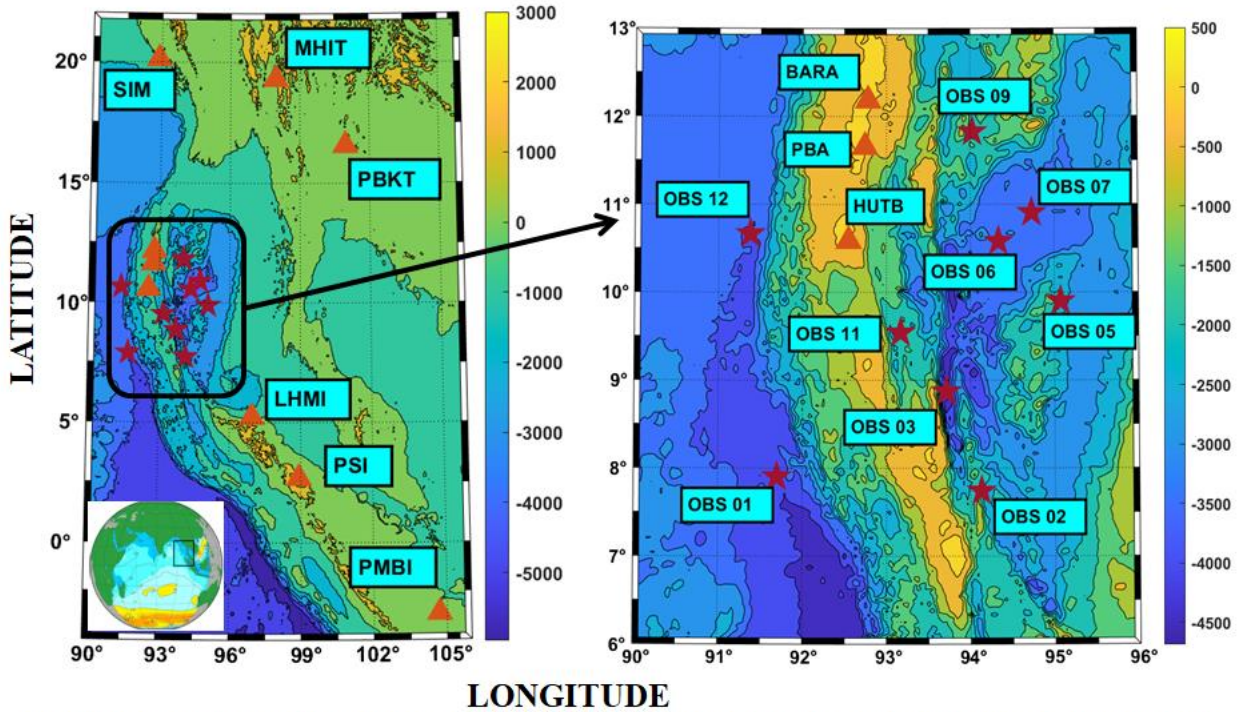


Figure 1: Location map of study area. Stars are OBS stations and triangles are land stations. A zoom out of the study location is shown in inset.

Figure 2

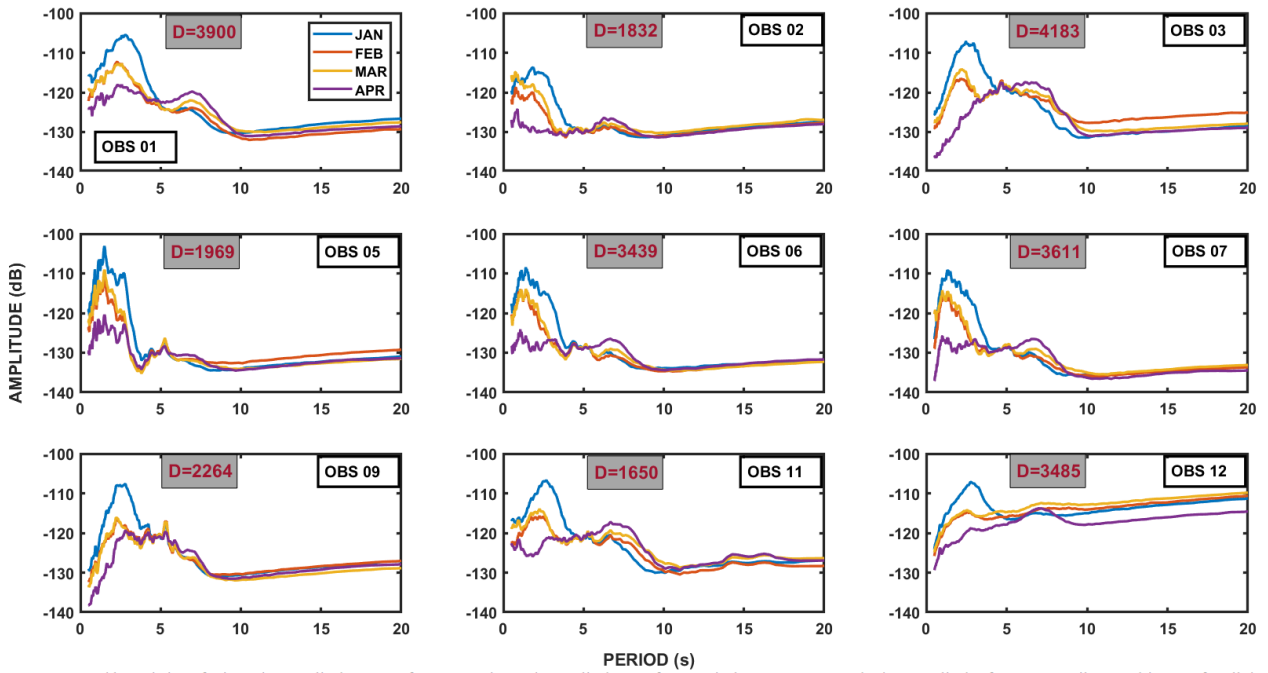


Figure 2: Monthly variation of microseism amplitude spectra for OBS stations. The amplitudes are from vertical component. Legends show amplitudes for Jan to April. Legend is same for all the subplots. D represents depth in meters.

Figure 3

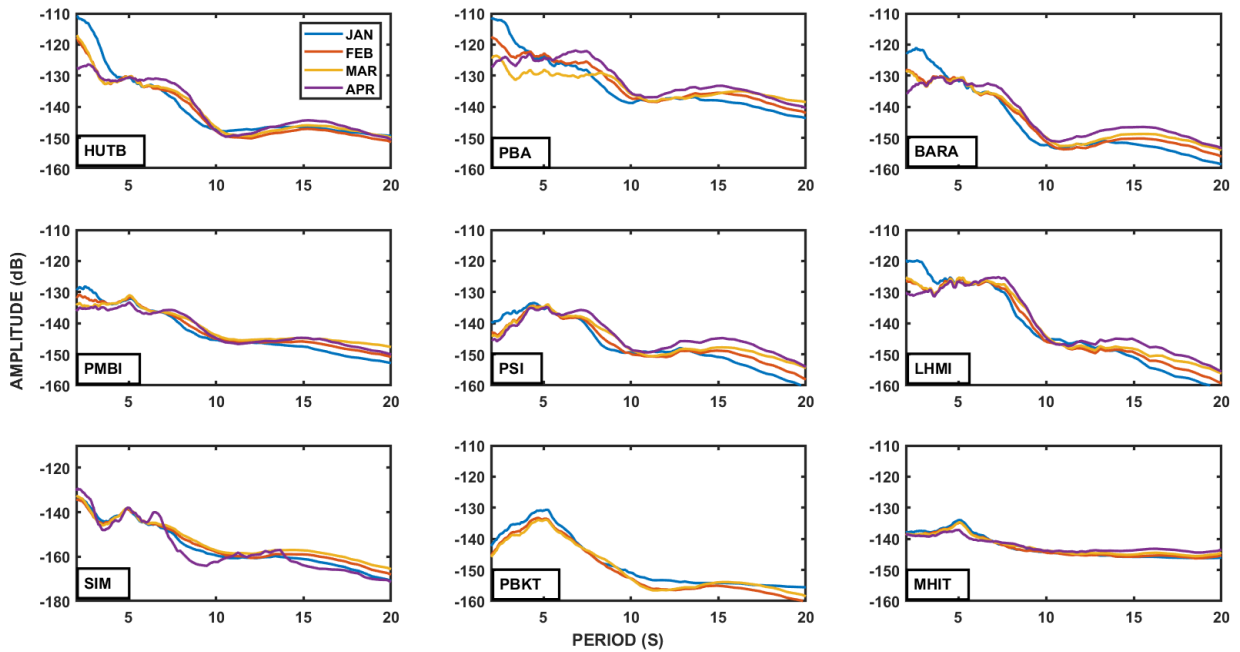


Figure 3: Monthly variation of microseism amplitude spectra for LAND stations. The amplitudes are from vertical component. Legends show amplitudes for Jan to April. Legend is same for all the subplots.

Figure 4

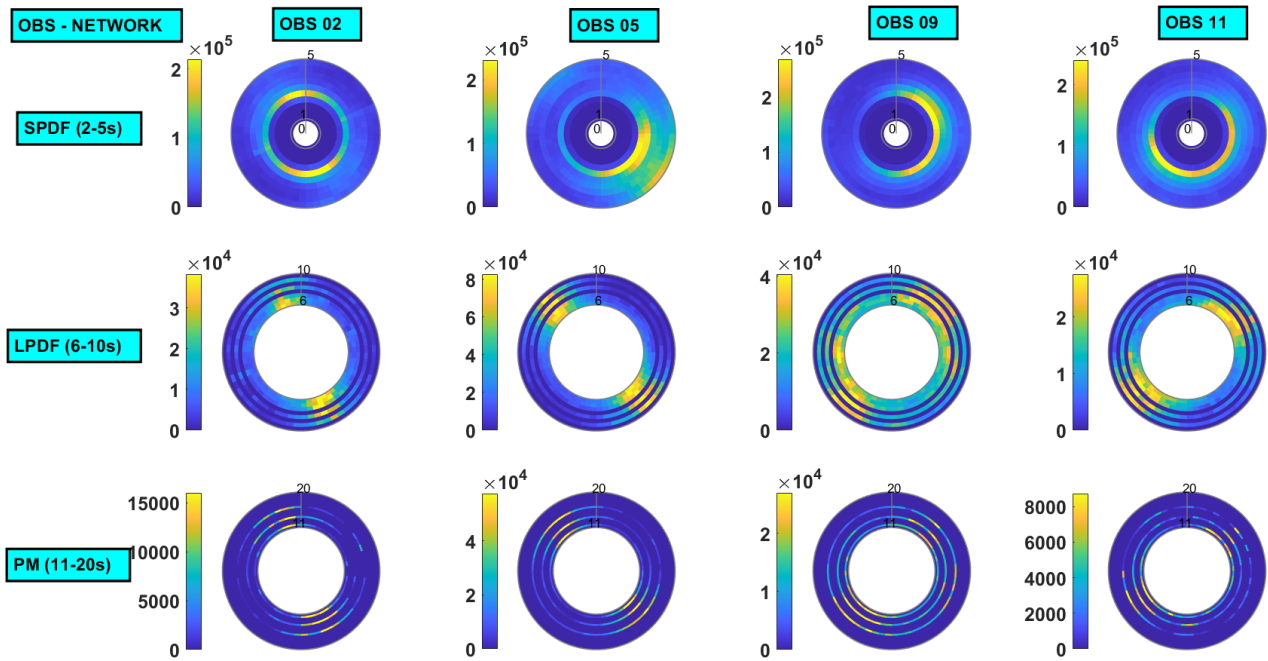


Figure 4: Polarization spectra for OBS stations. Measurements are for entire duration of deployment. Color scale represents number of polarized signals.

Figure 5

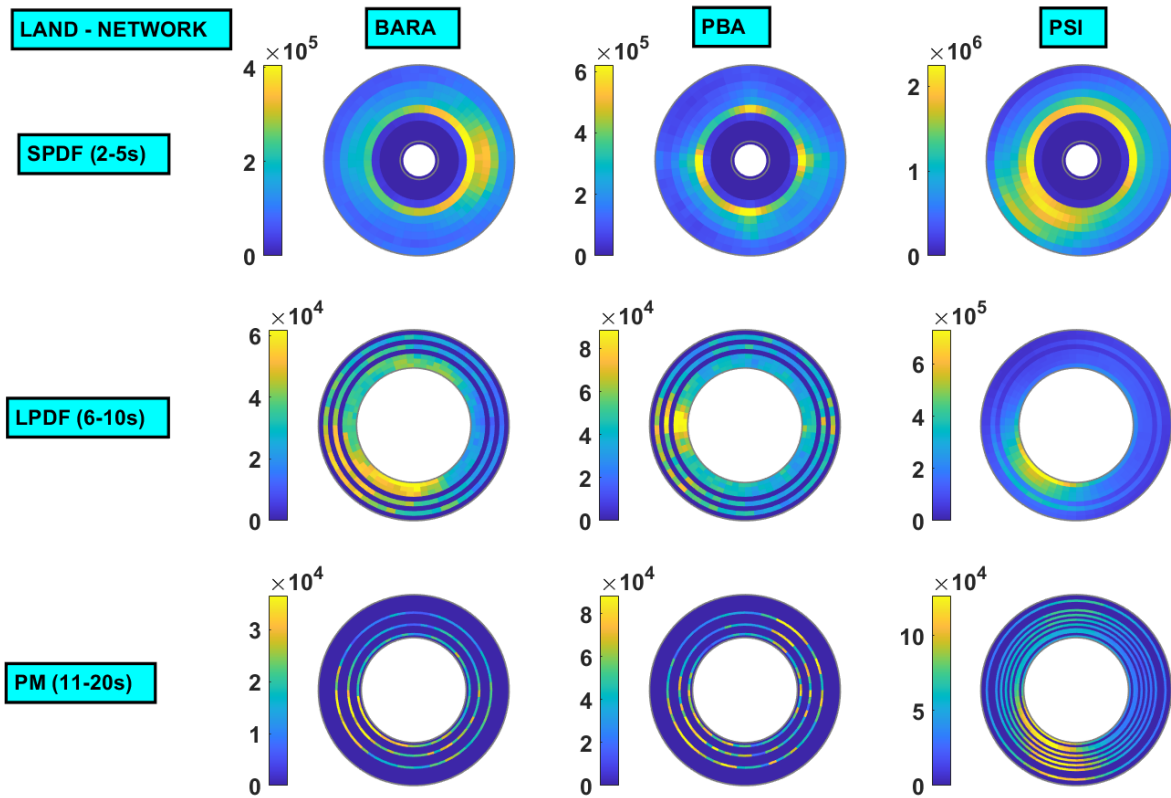


Figure 5: Polarization spectra for LAND stations. Measurements are for entire duration of deployment. Color scale represents number of polarized signals.

Figure 6

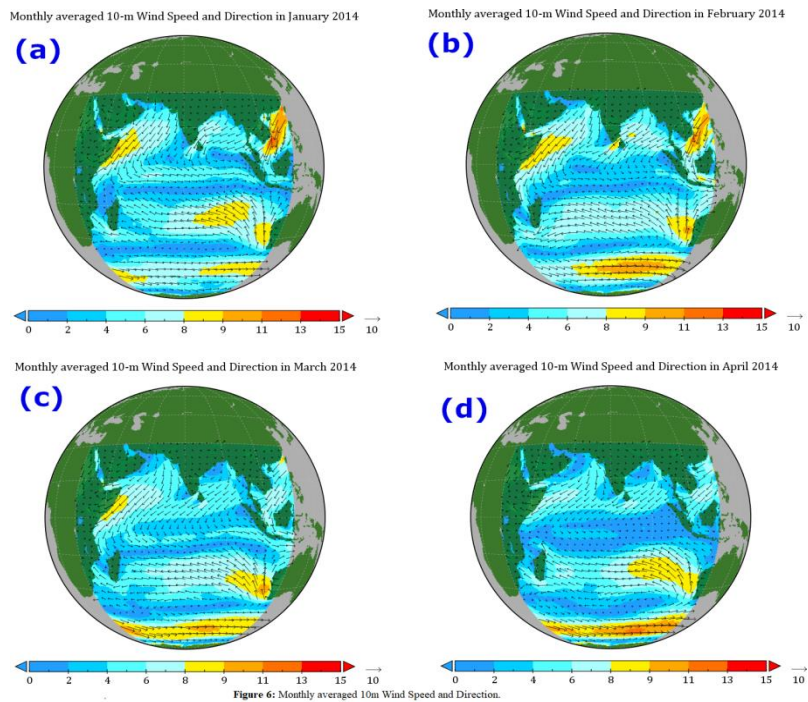
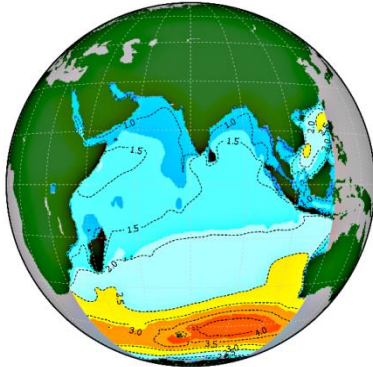
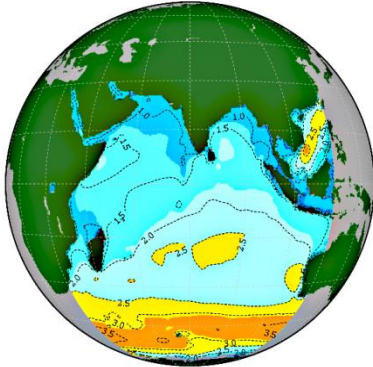


Figure 7

Monthly averaged Significant Wave Height (in meters) in January 2014 Monthly averaged Significant Wave Height (in meters) in February 2014



Monthly averaged Significant Wave Height (in meters) in March 2014

Monthly averaged Significant Wave Height (in meters) in April 2014

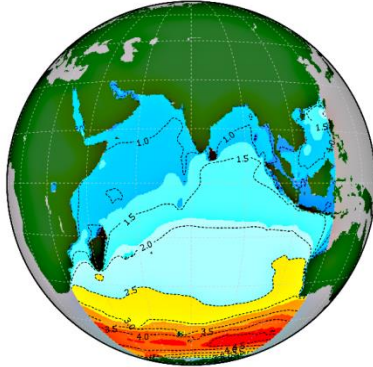
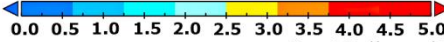
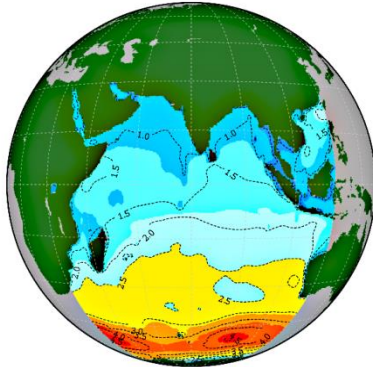


Figure 7: Monthly averaged Significant Wave Heights.

Figure 8

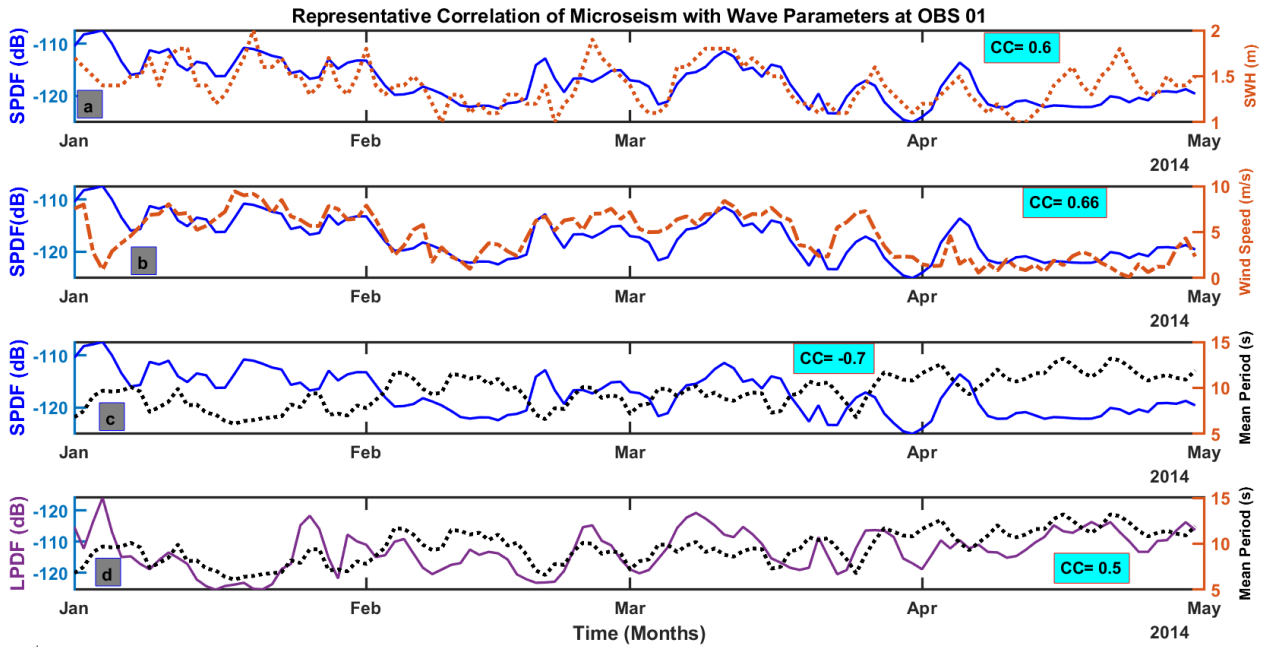


Figure 8: Representative Correlation of microseism (solid lines) with ocean wave parameters (a) SPDF Vs SWH (b) SPDF Vs Wind Speed (c) SPDF Vs Mean Period (d) LPDF Vs Mean Period.

Table 1

WAVE PARAMETERS	OBS01			OBS02			OBS03			OBS05		
	SPDF	LPDF	PM	SPDF	LPDF	PM	SPDF	LPDF	PM	SPDF	LPDF	PM
Wind Speed	0.67	-0.26	0.05	0.74	-0.28	-0.10	0.80	-0.36	-0.02	0.77	-0.38	-0.18
Sea Level Pressure	0.46	-0.21	0.00	0.50	-0.27	-0.26	0.60	-0.40	-0.20	0.69	-0.47	-0.31
Significant Wave Height	0.60	0.28	0.17	0.73	-0.06	-0.22	0.80	-0.12	-0.01	0.74	-0.30	-0.33
Mean Wave Period	-0.70	0.49	-0.02	-0.78	0.40	-0.03	-0.81	0.57	0.01	-0.73	0.50	0.09
Mean Wave Direction	-0.63	0.45	0.08	-0.75	0.38	0.07	-0.76	0.53	0.09	-0.53	0.31	0.11
Signification wave height of Total Swell	0.21	0.55	0.22	0.53	-0.05	-0.17	0.58	0.00	0.13	0.20	0.14	-0.08
Significant wave height of Wind-Waves	0.67	-0.27	0.01	0.78	-0.27	-0.11	0.82	-0.39	-0.08	0.80	-0.45	-0.22
Significant wave height of first swell partition	-0.04	0.49	0.09	0.24	0.04	-0.24	0.61	-0.22	0.01	0.06	0.12	-0.07
Significant wave height of second swell partition	0.42	0.04	0.23	0.43	-0.02	-0.03	0.20	0.28	0.29	0.29	0.07	0.06
Significant wave height of third swell partition	0.11	0.00	0.10	-0.03	0.20	0.14	-0.15	0.34	0.10	0.01	0.11	-0.08
Mean Period of Total Swell	-0.62	0.53	-0.02	-0.66	0.39	-0.09	-0.67	0.48	-0.07	-0.55	0.44	0.08
Mean wave period of first swell partition	-0.04	-0.02	-0.12	-0.17	0.11	-0.03	0.01	-0.02	-0.10	0.07	-0.10	-0.10
Mean wave period of second swell partition	0.19	-0.09	0.06	0.30	0.04	0.07	0.23	-0.05	-0.11	0.25	-0.11	-0.05
Mean wave period of third swell partition	0.03	0.15	0.10	0.09	-0.04	-0.08	0.06	0.00	0.02	0.07	0.10	0.03
Mean Direction of Total Swell	-0.39	0.26	-0.01	-0.69	0.33	0.04	-0.64	0.39	0.11	-0.46	0.27	0.10
Mean wave direction of first swell partition	-0.23	0.16	-0.05	-0.49	0.23	0.02	-0.22	0.32	0.33	-0.22	0.21	0.12
Mean wave direction of second swell partition	-0.18	0.16	0.02	-0.23	0.12	0.01	-0.20	0.09	0.06	-0.29	0.21	0.03
Mean wave direction of third swell partition	0.22	0.06	-0.06	-0.01	-0.12	-0.22	-0.02	-0.06	-0.22	0.04	-0.06	-0.05

	OBS06			OBS07			OBS09			OBS11			OBS12		
	SPDF	LPDF	PM	SPDF	LPDF	PM	SPDF	LPDF	PM	SPDF	LPDF	PM	SPDF	LPDF	PM
	0.75	-0.33	0.00	0.71	-0.37	0.10	0.71	-0.17	0.09	0.73	-0.40	-0.19	0.71	0.17	0.39
	0.69	-0.24	0.03	0.69	-0.30	0.06	0.67	-0.22	0.02	0.60	-0.32	-0.15	0.57	0.18	0.33
	0.74	0.02	0.01	0.68	-0.03	-0.01	0.73	0.00	0.05	0.72	-0.04	-0.09	0.38	0.01	-0.07
	-0.70	0.60	0.00	-0.67	0.56	-0.12	-0.68	0.37	-0.09	-0.77	0.65	0.20	-0.73	-0.10	-0.41
	-0.56	0.27	-0.06	-0.53	0.31	-0.02	-0.44	0.05	-0.12	-0.72	0.51	0.19	-0.53	0.07	-0.14
	0.31	0.26	-0.09	0.20	0.22	-0.04	0.36	0.05	-0.05	0.39	0.32	-0.01	0.09	-0.01	-0.21
	0.78	-0.28	0.03	0.71	-0.39	0.01	0.70	-0.14	0.07	0.75	-0.39	-0.18	0.66	0.08	0.28
	0.21	0.30	0.00	-0.04	0.29	-0.14	0.16	0.19	0.07	0.13	0.30	0.08	-0.23	-0.12	-0.33
	0.34	-0.23	-0.18	0.28	-0.08	0.06	0.27	-0.12	-0.15	0.57	-0.18	-0.20	0.45	0.21	0.25
	0.06	0.08	-0.14	0.22	0.09	0.19	0.14	-0.13	-0.10	0.07	0.14	0.00	0.20	0.08	0.12
	-0.60	0.63	0.00	-0.56	0.50	-0.16	-0.57	0.42	-0.07	-0.68	0.69	0.18	-0.67	-0.05	-0.38
	-0.13	0.42	-0.01	0.03	0.13	-0.06	-0.10	0.30	0.02	-0.12	0.17	-0.02	-0.29	0.22	0.01
	0.31	-0.27	0.00	0.28	-0.20	-0.12	0.36	-0.19	0.02	0.40	-0.21	0.00	0.10	-0.05	-0.03
	-0.18	-0.13	-0.13	-0.04	0.14	0.00	-0.12	-0.03	-0.06	0.10	-0.02	-0.01	-0.03	-0.01	0.05
	-0.46	0.13	-0.14	-0.47	0.27	0.02	-0.42	0.08	-0.10	-0.52	0.42	0.07	-0.22	0.12	0.00
	-0.35	0.21	-0.09	-0.38	0.17	0.04	-0.23	0.10	-0.05	-0.59	0.39	0.06	-0.23	0.20	0.09
	-0.07	0.25	0.00	-0.31	0.34	0.11	-0.37	0.26	-0.04	-0.03	0.19	0.21	-0.25	-0.22	-0.30
	0.01	0.06	0.20	0.13	0.01	0.00	0.15	-0.01	0.18	0.09	-0.19	-0.22	-0.16	-0.13	-0.14

	BARA			PBA		
	SPDF	LPDF	PM	SPDF	LPDF	PM
	0.63	-0.36	-0.41	0.67	-0.22	0.12
	0.64	-0.34	-0.39	0.68	-0.20	0.09
	0.72	-0.27	-0.40	0.74	-0.12	0.16
	-0.67	0.56	0.54	-0.68	0.45	0.05
	-0.44	0.26	0.28	-0.52	0.13	-0.10
	0.62	-0.29	-0.38	0.64	-0.18	0.03
	0.60	-0.33	-0.34	0.62	-0.16	0.21
	0.56	-0.35	-0.37	0.60	-0.23	0.06
	0.15	0.17	0.01	0.13	0.11	-0.07
	-0.09	0.27	0.08	-0.09	0.21	-0.12
	-0.53	0.54	0.51	-0.52	0.48	0.17
	0.01	0.03	0.04	-0.01	0.09	0.22
	0.33	-0.13	-0.20	0.35	-0.09	-0.03
	-0.08	0.05	-0.02	-0.03	0.07	-0.09
	-0.50	0.32	0.41	-0.50	0.24	0.09
	-0.26	0.18	0.31	-0.25	0.13	0.12
	-0.02	0.17	0.13	0.05	0.17	0.14
	0.14	-0.12	-0.09	0.14	-0.12	0.03

Supplementary Material for

“Possible linkages between Microseisms in the Andaman-Nicobar region and Swells in the South Indian Ocean”

by

R. Reddy^{1,2}, P. Dewangan^{1*}, Prasad. K. Bhaskaran² and P.N.S. Roy²

¹CSIR-National Institute of Oceanography, Dona Paula, Goa – India – 403004.

²Indian Institute of Technology Kharagpur, Kharagpur, West Bengal, India – 721302

*Corresponding author Email: pdewangan@nio.org

The document contains the supporting figures and movies for the above manuscript.

List of Supplemental Figure Captions

Figure S1: Monthly variation of Polarization spectra for OBS02 station. Color scale represents number of polarized signals.

Figure S2: Monthly variation of Polarization spectra for OBS05 station. Color scale represents number of polarized signals.

Figure S3: Monthly variation of Polarization spectra for OBS09 station. Color scale represents number of polarized signals.

Figure S4: Monthly variation of Polarization spectra for OBS11 station. Color scale represents number of polarized signals.

Figure S5: Monthly variation of Polarization spectra for BARA station. Color scale represents number of polarized signals.

Figure S6: Monthly variation of Polarization spectra for PBA station. Color scale represents number of polarized signals.

Figure S7: Monthly variation of Polarization spectra for PSI station. Color scale represents number of polarized signals.

Figure S8: Monthly averaged mean wave period extracted from ERA-5 dataset.

Figure S9: Monthly averaged mean wave direction extracted from ERA-5 dataset.

Data and resources

The ocean-bottom seismometer (OBS) data were acquired in the Andaman–Nicobar region under Council of Scientific and Industrial Research - Geodynamics and Earthquake generating processes in NE India and Andaman Subduction zone (CSIR-GENIAS) Project. The waveform data for the BARA station were provided by Earth System Sciences Organization - Indian National Centre for Ocean Information Services (ESSO-INCOIS), Ministry of Earth Sciences, Government of India on 22nd August 2016. Earthquake data for the continental stations were compiled from the IRIS Data Management Center (IRISDMC). The monitoring network comprises of Thai Seismic Monitoring Network (MHIT and PBKT), GEOFONE GE Seismic Network (LHMI and PMBI), GEOFONE IA Seismic Network (PSI), Malaysian National Seismic Network (KUM) and Myanmar National Seismic Network (SIM). All the figures are made using MATLAB R2019b. M-Map toolbox was used for plotting (Pawlowicz, 2020). Polfre code was used for the polarization analysis.

Figure S1

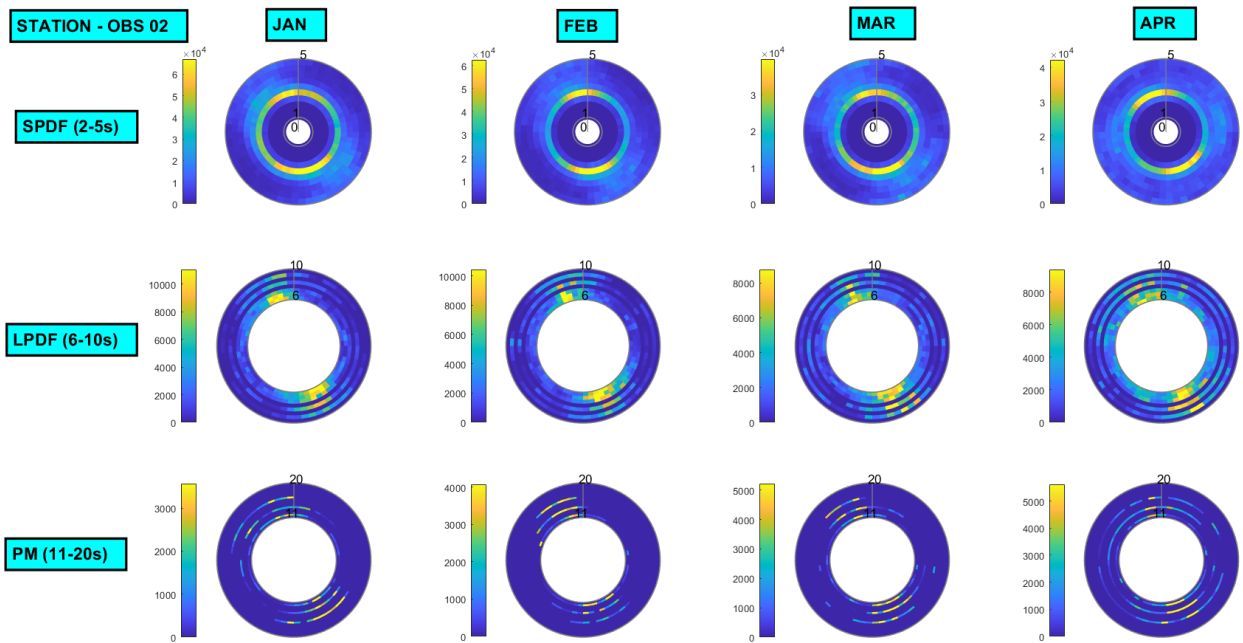


Figure S1. Monthly variation of Polarization spectra for OBS02 station. color scale represents number of polarized signals

Figure S2

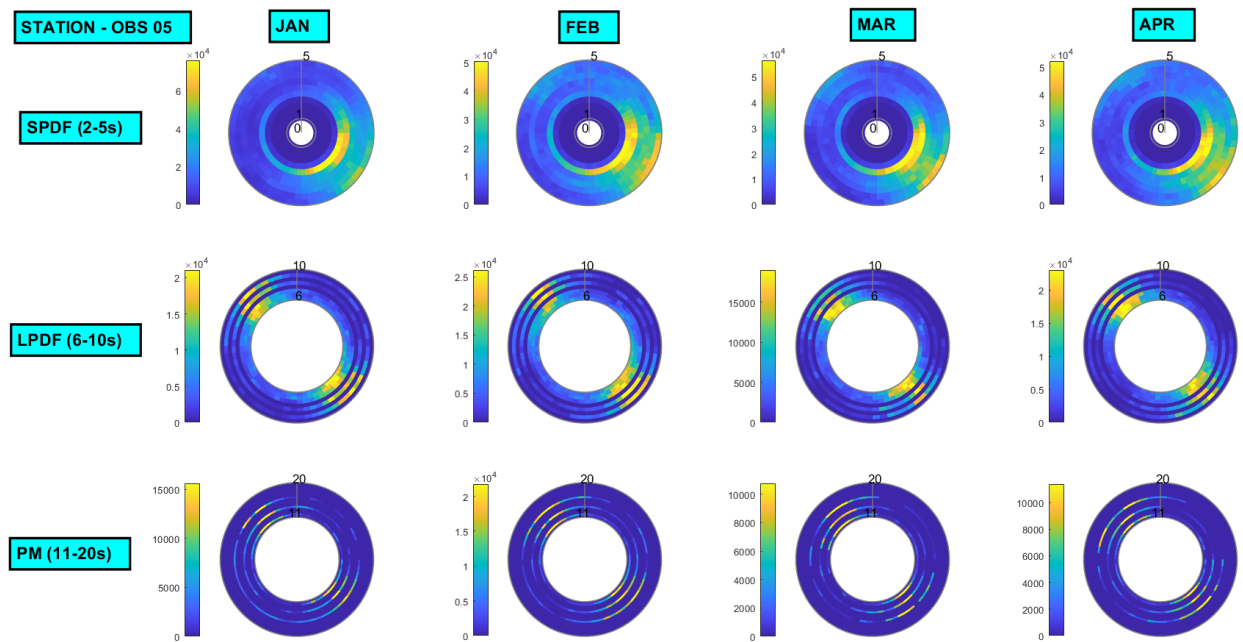


Figure S2. Monthly variation of Polarization spectra for OBS05 station. Color scale represents number of polarized signals

Figure S3

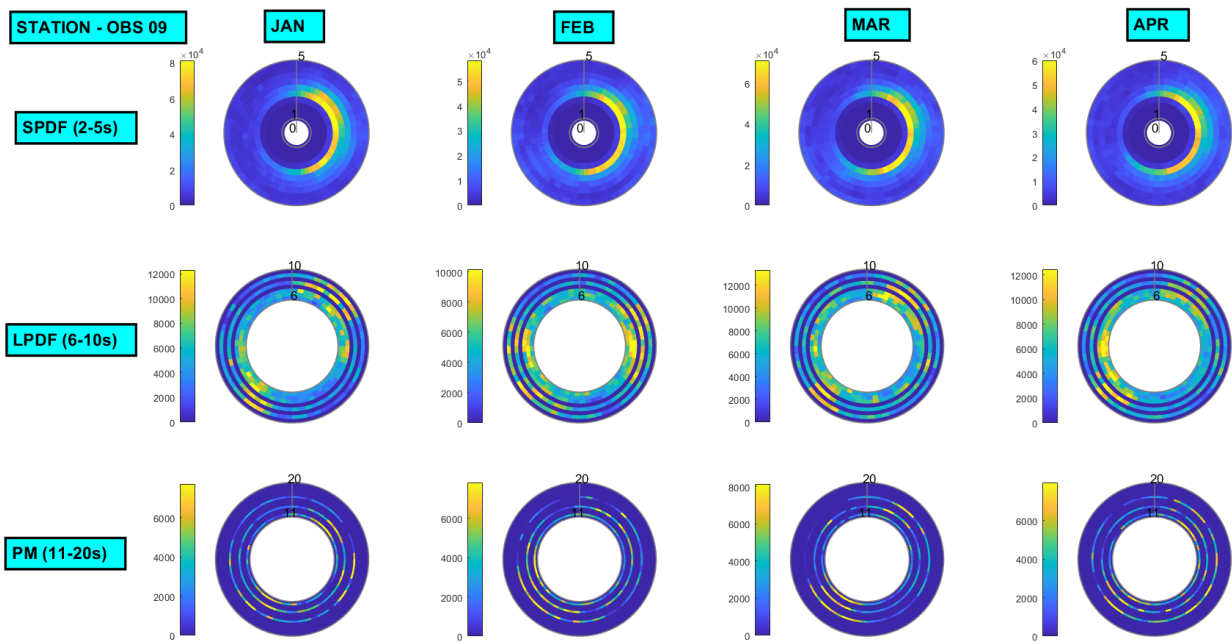


Figure S3. Monthly variation of Polarization spectra for OBS09 station. Color scale represents number of polarized signals

Figure S4

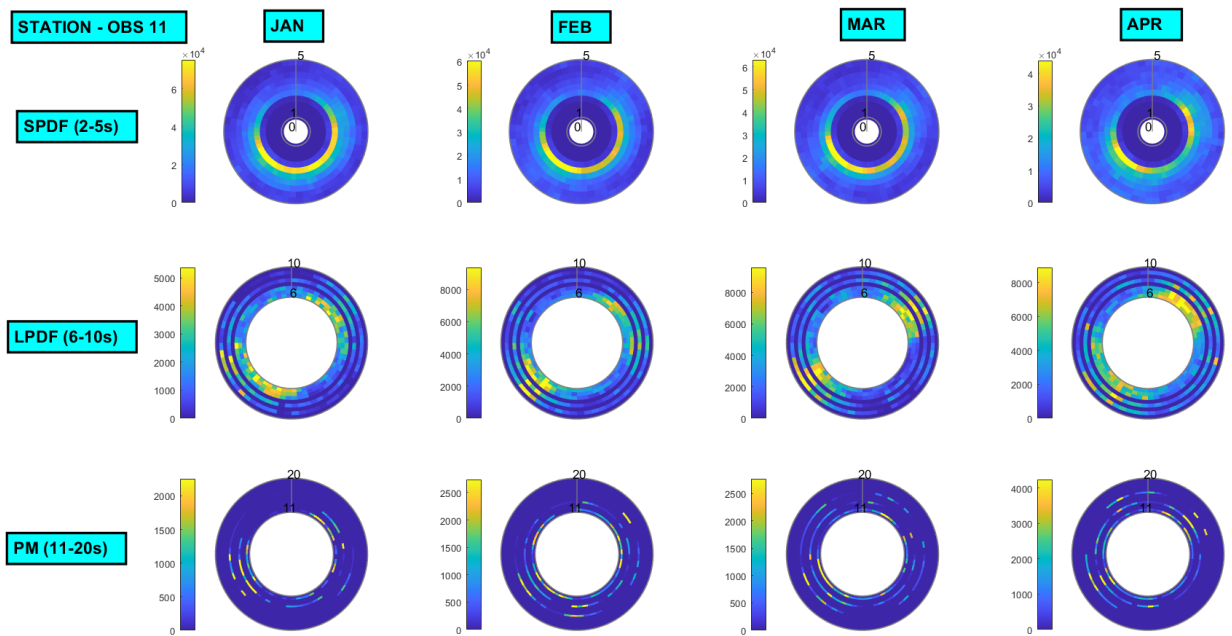


Figure S4. Monthly variation of Polarization spectra for OBS11 station. Color scale represents number of polarized signals

Figure S5

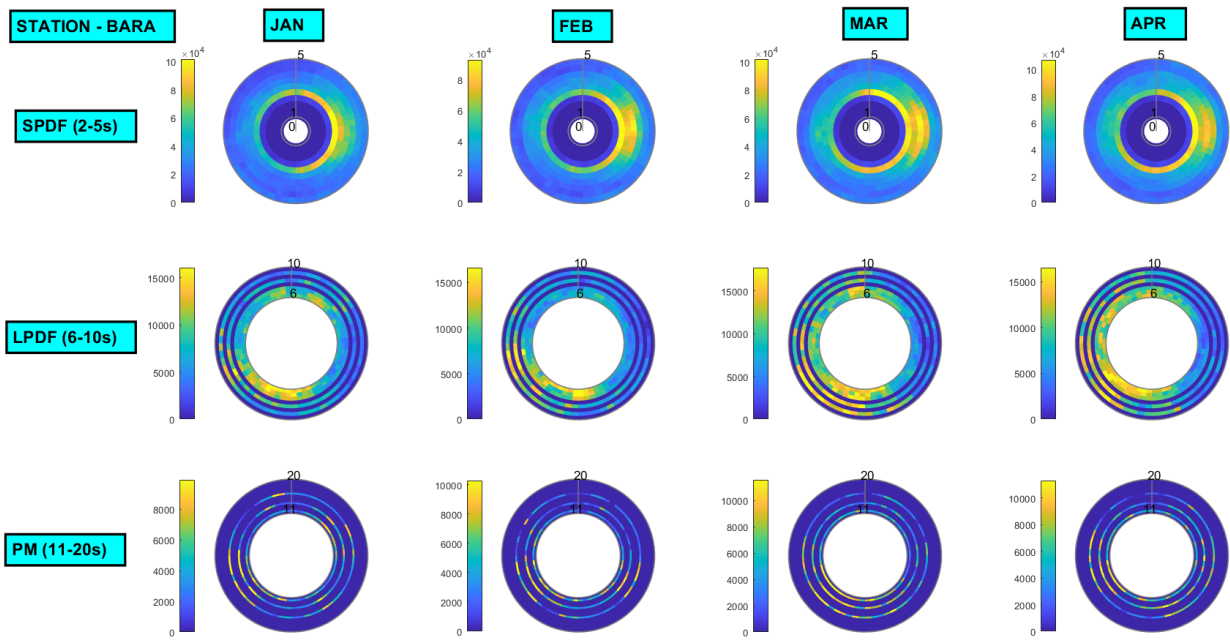


Figure S5. Monthly variation of Polarization spectra for BARA station. Color scale represents number of polarized signals

Figure S6

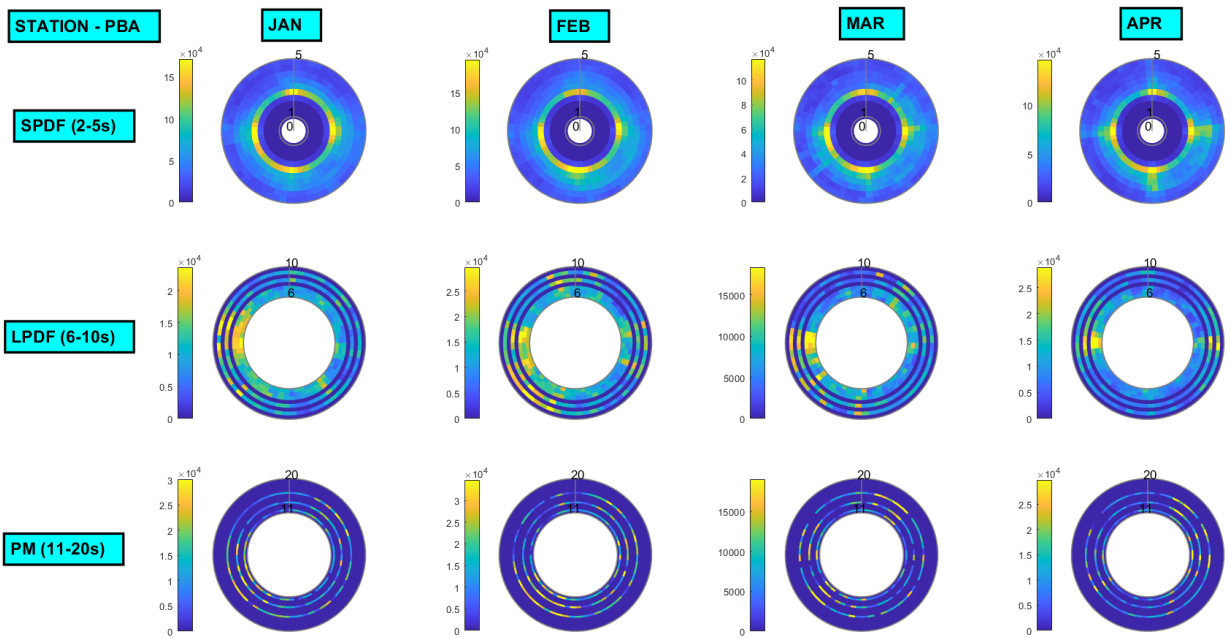


Figure S6. Monthly variation of Polarization spectra for PBA station. Color scale represents number of polarized signals

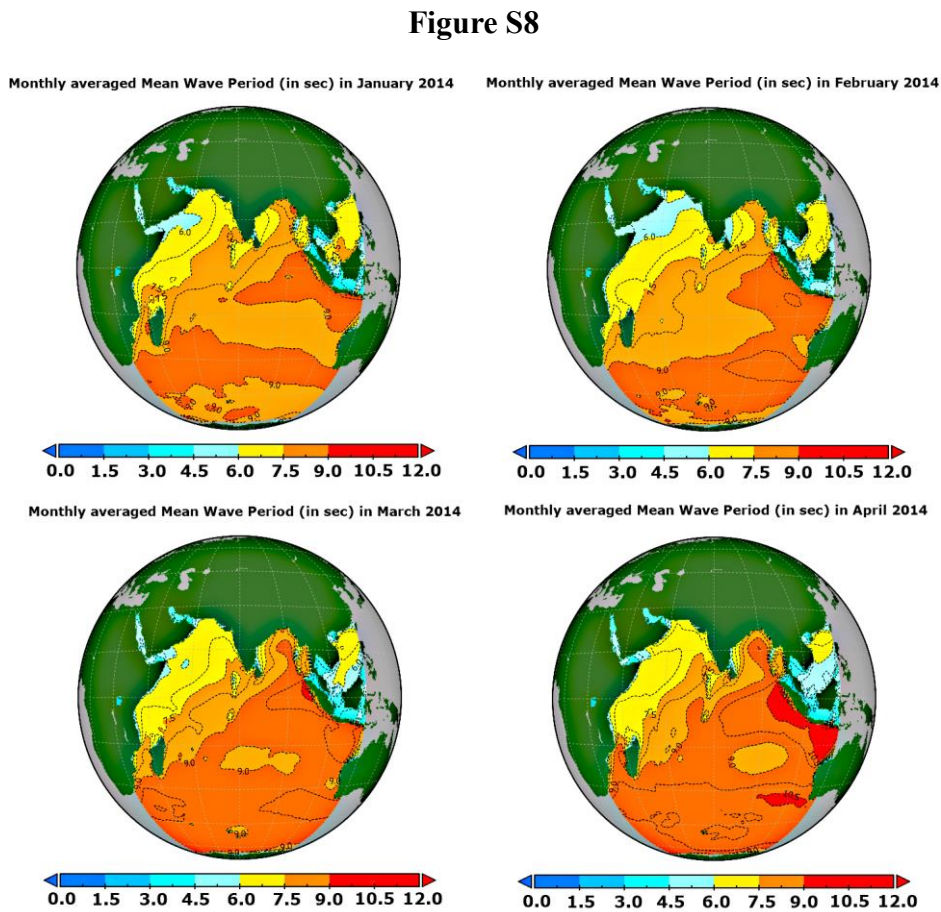
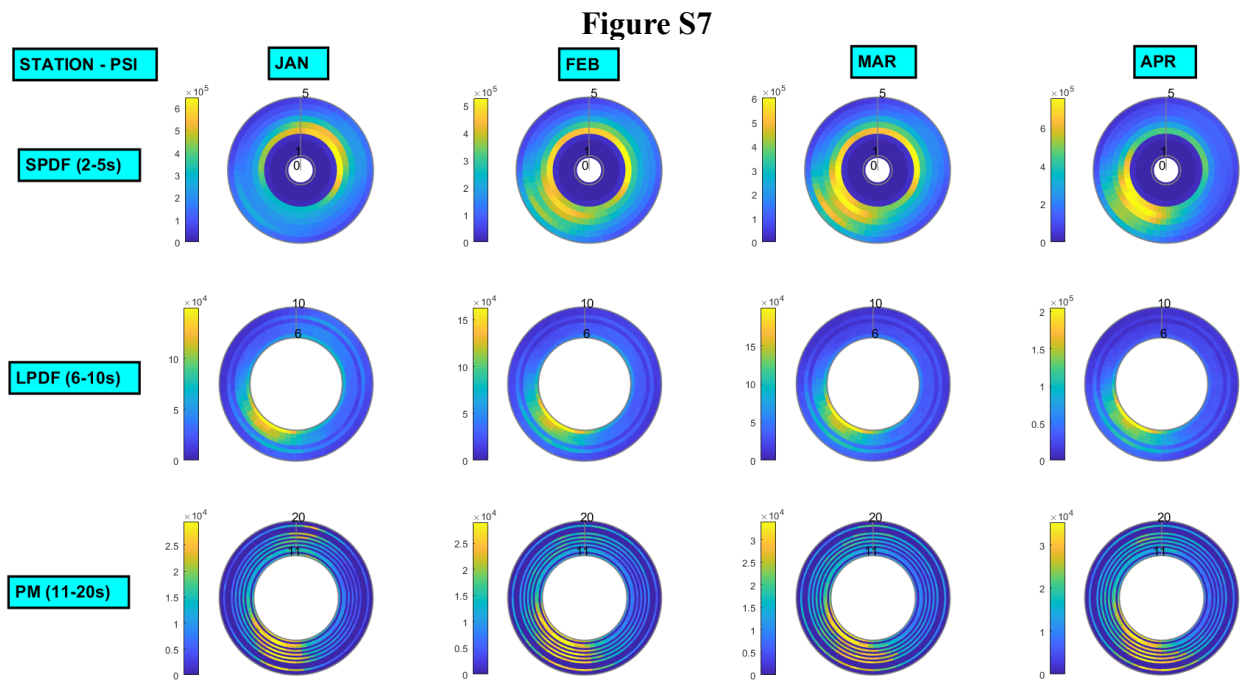
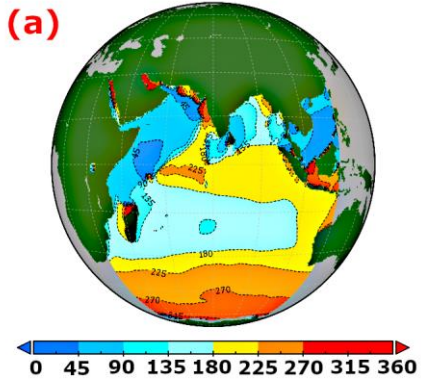
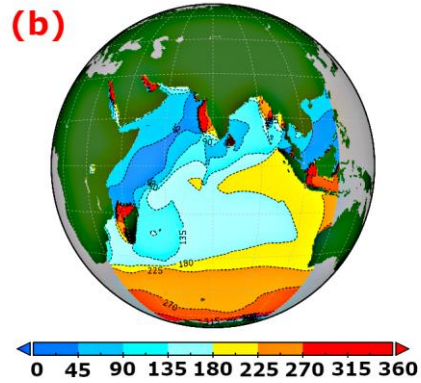


Figure S9

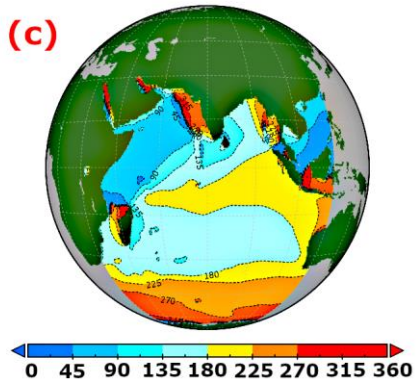
Monthly averaged Mean Wave Direction (in $^{\circ}$) in January 2014



Monthly averaged Mean Wave Direction (in $^{\circ}$) in February 2014



Monthly averaged Mean Wave Direction (in $^{\circ}$) in March 2014



Monthly averaged Mean Wave Direction (in $^{\circ}$) in April 2014

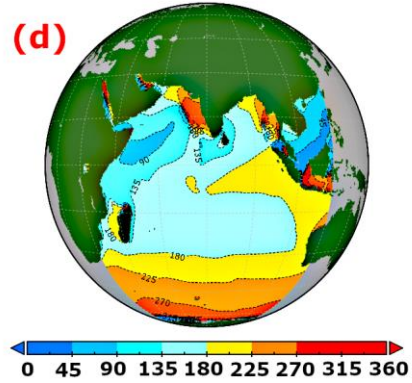


Figure S9. Monthly averaged Mean Wave direction